DOT/FAA/TCTT/25-19

Federal Aviation Administration
William J. Hughes Technical Center
Aviation Research Division
Atlantic City International Airport
New Jersey 08405

Ductile Fracture of Ti-6Al-4V Titanium Alloy Under Compressive Stress States

May 2025

Technical Thesis

The research described in this report was funded by the FAA as part of its mission to improve aircraft safety. The views and opinions expressed are those of the author alone and do not necessarily represent the views of the FAA. The FAA assumes no liability for the contents or use thereof. The FAA has not edited or modified the contents of the report in any manner.

U.S. Department of Transportation
Federal Aviation Administration

NOTICE

This document is disseminated under the sponsorship of the U.S. Department of Transportation in the interest of information exchange. The U.S. Government assumes no liability for the contents or use thereof. The U.S. Government does not endorse products or manufacturers. Trade or manufacturers' names appear herein solely because they are considered essential to the objective of this report. The findings and conclusions in this report are those of the author(s) and do not necessarily represent the views of the funding agency. This document does not constitute FAA policy. Consult the FAA sponsoring organization listed on the Technical Documentation page as to its use.

This report is available at the Federal Aviation Administration William J. Hughes Technical Center's Full-Text Technical Reports page: actlibrary.tc.faa.gov in Adobe Acrobat portable document format (PDF).

Form DOT F 1700.7 (8-72) Reproduction of completed page authorized

1. Report No.	2. Government Accession No.	3. Recipient's Catalog No.
DOT/FAA/TCTT/25-19		

4. Title and Subtitle	5. Report Date
Ductile Fracture of Ti-6Al-4V Titanium Alloy Under Compressive Stress States	May 2025
	6. Performing Organization Code

7. Author(s)	8. Performing Organization Report No.
Ethan J. White	

9. Performing Organization Name and Address	10. Work Unit No. (TRAIS)
University of Dayton 300 College Park Dayton, OH 45469	11. Contract or Grant No. 692M151940011

12. Sponsoring Agency Name and Address	13. Type of Report and Period Covered
Federal Aviation Administration Aircraft Certification Service Policy and Innovation Division (AIR-600) 800 Independence Avenue SW Washington, DC 20591	Technical Thesis
	14. Sponsoring Agency Code AIR-625

15. Supplementary Notes

The FAA William J. Hughes Technical Center Aviation Research Division COR was Daniel Cordasco.

16. Abstract

A notoriously challenging modeling and simulation problem is the impact physics of jet engine debris striking the engine case during a fan blade-out or rotor-burst event. The multiplicity of potential failure modes resulting from the impact and subsequent penetration of high-speed engine fragments advances the challenge. The ductile fracture model must be robust to account for all potential failure modes. The failure locus, a key ingredient in many state-of-the-art ductile fracture models, is a three-dimensional surface plot of the equivalent plastic strain at fracture as a function of the state of stress, quantified by the stress triaxiality and Lode parameter. Standard mechanical tests are generally used to populate the failure locus, but standard tests can only capture a limited window of stress states. This limited window potentially leaves important regions of the failure locus unpopulated. For instance, a significant body of previous research suggests that fracture will not occur above a stress triaxiality of 0.33 (known as the "cut-off" value). However, recent ballistic impact simulations involving 12.7-mm-thick Ti-6Al-4V titanium alloy plates predict large positive (compressive) triaxialities in the vicinity of the adiabatic shear band. These results not only suggest the potentially unanticipated importance of the positive triaxiality (compressive) region of Lode-triaxiality stress space, but also the need to experimentally revisit previous interpretations of the "cut-off" value of the triaxiality. Toward that end, this thesis investigates the ductile fracture of 6.35-mm-thick and 12.7-mm-thick Ti-6Al-4V titanium plate under compressive stress states. Specifically, our experimental plan is designed to interrogate the quasi-static ductile fracture behavior of Ti-6Al-4V plate under complex, highly triaxial, compression-dominated stress states. To achieve this, our testing program employs a series of cylindrical compression specimens with asymmetric features and/or geometric irregularities including vertical through-holes, 45-degree through-holes, horizontal through holes, a 45-degree slot, and a spherical recess. This test series is intended to complement previous ductile fracture experiments performed on the same lot of 12.7-mm-thick Ti-6Al-4V plate stock. Stereo digital image correlation is used to measure surface displacements and compute full-field strains at and near the fracture location. The experimental results are coupled with numerical simulations in LS-DYNA to calculate the stress state evolution and fracture strain at the site of fracture initiation. Weighted-average triaxialities of 0.61, 0.72, and 0.81 are reported for the specimens with through-holes, placing these experiments among the most compression-dominated in the literature.

17. Key Words	18. Distribution Statement
Ti-6Al-4V, Impact, LS-DYNA, Dynamic models, Failure, Fracture, Plasticity, Simulation, Finite element method, Triaxiality, Lode, Compression	This document is available to the U.S. public through the National Technical Information Service (NTIS), Springfield, Virginia 22161. This document is also available from the Federal Aviation Administration William J. Hughes Technical Center at actlibrary.tc.faa.gov.

19. Security Classif. (of this report)	20. Security Classif. (of this page)	21. No. of Pages	22. Price
Unclassified	Unclassified		

DUCTILE FRACTURE OF Ti-6Al-4V TITANIUM ALLOY UNDER COMPRESSIVE STRESS STATES

Thesis

Submitted to

The School of Engineering of the

UNIVERSITY OF DAYTON

In Partial Fulfillment of the Requirements for

The Degree of

Master of Science in Aerospace Engineering

By

Ethan J. White

Dayton, Ohio

May, 2025

DUCTILE FRACTURE OF Ti-6Al-4V TITANIUM ALLOY UNDER COMPRESSIVE STRESS STATES

Name: White, Ethan J.

APPROVED BY:

Robert L. Lowe, Ph.D.
Thesis Committee Chair
Associate Professor, Mechanical and Aerospace Engineering

Jeremy D. Seidt, Ph.D.
Committee Member
Research Associate Professor, The Ohio State University

Kelly S. Carney, Ph.D.
Committee Member
Engineering Consultant, George Mason University

Abdullah Al Amin, Ph.D.
Committee Member
Assistant Professor, Mechanical and Aerospace Engineering

Leyu Wang, Ph.D.
Committee Member
Research Assistant Professor, George Mason University

ABSTRACT

DUCTILE FRACTURE OF Ti-6Al-4V TITANIUM ALLOY UNDER COMPRESSIVE STRESS STATES

Name: White, Ethan J.
University of Dayton

Advisor: Dr. Robert L. Lowe

A notoriously challenging modeling and simulation problem is the impact physics of jet engine debris striking the engine case during a fan blade-out or rotor-burst event. The multiplicity of potential failure modes resulting from the impact and subsequent penetration of high-speed engine fragments advances the challenge. The ductile fracture model must be robust to account for all potential failure modes. The failure locus, a key ingredient in many state-of-the-art ductile fracture models, is a three-dimensional surface plot of the equivalent plastic strain at fracture as a function of the state of stress, quantified by the stress triaxiality and Lode parameter. Standard mechanical tests are generally used to populate the failure locus, but standard tests can only capture a limited window of stress states. This limited window potentially leaves important regions of the failure locus unpopulated.

For instance, a significant body of previous research suggests that fracture will not occur above a stress triaxiality of 0.33 (known as the "cut-off" value). However, recent ballistic impact simulations involving 12.7-mm-thick Ti-6Al-4V titanium alloy plates predict large positive (compressive) triaxialities in the vicinity of the adiabatic shear band. These results not only suggest the potentially unanticipated importance of the positive triaxiality (compressive) region of Lode-triaxiality stress space, but also the need to experimentally revisit

previous interpretations of the "cut-off" value of the triaxiality. Toward that end, this thesis investigates the ductile fracture of 6.35-mm-thick and 12.7-mm-thick Ti-6Al-4V titanium plate under compressive stress states. Specifically, our experimental plan is designed to interrogate the quasi-static ductile fracture behavior of Ti-6Al-4V plate under complex, highly triaxial, compression-dominated stress states. To achieve this, our testing program employs a series of cylindrical compression specimens with asymmetric features and/or geometric irregularities including vertical through-holes, 45-degree through-holes, horizontal through-holes, a 45-degree slot, and a spherical recess. This test series is intended to complement previous ductile fracture experiments performed on the same lot of 12.7-mm-thick Ti-6Al-4V plate stock. Stereo digital image correlation is used to measure surface displacements and compute full-field strains at and near the fracture location. The experimental results are coupled with numerical simulations in LS-DYNA to calculate the stress state evolution and fracture strain at the site of fracture initiation. Weighted-average triaxialities of 0.61, 0.72, and 0.81 are reported for the specimens with through-holes, placing these experiments among the most compression-dominated in the literature.

Dedicated to my family and friends

ACKNOWLEDGMENTS

First and foremost, I would like to express my deepest gratitude to my family. Their unwavering love, patience, and support have been the cornerstone of my academic journey. To my parents, Terry and Sandy White, thank you for instilling in me the values of hard work and perseverance. Your belief in me, even during the most challenging moments, gave me the strength to keep going. To my siblings, Colin, Kylie, Maddie, Ella, Katie, and Mandy, thank you for your encouragement, your laughs, and your ability to push me to achieve great things. I would especially like to thank my brother Colin, for being my sounding board, your fresh perspective on ideas, helping me unwind, and talking about sports all the time. To my friends, thank you for being the perfect distraction when I needed to take a break, you all ensured I never lost sight of the importance of relaxation and fun.

I would also like to extend my heartfelt appreciation to my advisor, Dr. Robert Lowe, for his exceptional guidance, insightful feedback, and continuous support throughout the course of this research. Many of the milestones achieved through the duration of this project would not have been possible without him. His ability to challenge me to think critically and his attention to detail not only improved the quality of my work, but has grown my abilities as a researcher. Thank you for your unwavering commitment to my success and for being a role model of professionalism and academic excellence. This thesis would not have been possible without your mentorship. Thank you also to my co-advisor, Dr. Jeremy Seidt, for your mentorship, training, and advice. I am also grateful to Dr. Leyu (Doug) Wang, Dr. Kelly Carney, and Dr. Abdullah Al Amin for their guidance and insight as members of my masters advisory committee.

Thank you to all the members of the Behavior of Advanced Materials lab at the University of Dayton. I am grateful for the friendships and collaborative spirit that each of you brought to the lab environment. To the Dynamic Mechanics of Materials Lab at the Ohio State University, Grey McCarthy and Jerome Klein (and Dr. Jeremy Seidt and Dr. Amos Gilat), thank you for allowing me to come and do all my tests in your lab. Thank you for your technical support with digital image correlation and testing. Your help was a major factor in the successful execution of this work.

This research was funded by the Federal Aviation Administration and performed in collaboration with the National Aeronautics and Space Administration, George Mason University, and the Ohio State University. Thank you to all members of this team for your valuable input and guidance: Dr. Daniel Cordasco, Dr. Tom Vasko, Dr. Michael Pereira, Duane Revilock, Paul Du Bois, Dr. Cing-Dao (Steve) Kan, Dr. C.K. Park, Dr. Stefano Dolci, Dr. Amos Gilat, and Dr. Jeremy Seidt.

TABLE OF CONTENTS

LIST OF FIGURES

LIST OF TABLES

CHAPTER I

INTRODUCTION

1.1 Background and Motivation

Blade-off and rotor-burst events in gas turbine engines occur infrequently; however, they remain critical hazards that compromise the safety of commercial aircraft operations. Commercial aircraft are required by the Federal Aviation Administration (FAA) to be equipped with a containment system that prevents penetration of the engine case in the event of a blade-off or rotor-burst event. New, modified, and derivative jet engine designs are required to undergo full-scale destructive testing, where the most critical blade (fan blade) must be contained within the engine casing when separated from the disk at full thrust. The FAA requires commercial engine manufacturers to demonstrate this before certification (Title 14 of the Code of Federal Regulations (CFR) 33.94). Full-scale testing is both extremely expensive and difficult to conduct. To lessen the likelihood of a failed certification test (economically detrimental to the manufacturer), or in-flight failure (detrimental to human safety), predictive numerical simulations are needed.

Modeling and simulating the high-velocity impact (60–250 m/s) of engine fragments with the fan case during blade-off or rotor-burst events remains a significant technical challenge [1]. High strain rates, large plastic deformations, progressive damage, steep temperature gradients, and ductile fracture contribute to the complex impact-penetration physics and must be taken into account in the analysis. The ductile fracture model must be capable of accounting for multiple potential failure modes (plugging, petaling, and mixed-mode failure). The failure modes are directly related to the impact conditions (geometry, relative orientation, impact speed, and projectile and target material properties) and the subsequent state of stress at impact. Different impact conditions will lead to different states of stress

at impact and, inherently, different failure modes which must all be captured by the ductile fracture model.

1.2 Literature Review

The work of McClintock [2] and Rice and Tracey [3] provided theories of microscopic void nucleation, growth, and coalescence that inspired early damage indicator and ductile fracture initiation models for metals. First recognizing the role of voids in ductile fracture, McClintock [2] demonstrated that failure strain depends on the full state of stress rather than just the maximum principal stress. Using a microscopic void growth model, Rice and Tracey [3] demonstrated that the dilatational amplification (volumetric growth) of a spherical void increases exponentially with the far-field mean stress. A physics-based plasticity model was developed by Gurson [4] based on these ideas. This model had micro-scale porosity incorporated into the continuum constitutive model via an internal table. Tvergaard and Needleman [5] later modified Gurson's to couple damage and plasticity by accounting for ductile fracture through the dependence of the yield function on a critical void volume fraction. Gurson's plasticity model was modified countless times to account for ductile fracture and can be found in Refs. [6–8].

Continuum-scale phenomenological ductile fracture models that are inspired by void nucleation, growth and coalescence differ from the micromechanics-based Gurson-type models. However, within commercial finite element codes for structural-level analysis, these continuum-scale phenomenological ductile fracture models have proven popular and effective. Johnson and Cook [9], perhaps the most famous phenomenological ductile fracture model, provides a mathematical relationship between the equivalent plastic strain at fracture (common measure of ductility) and the stress triaxiality (normalized mean stress,

generally defined as the ratio of the mean (hydrostatic) stress to the equivalent (e.g., von Mises) stress). Hancock and Mackenzie [10] and Mackenzie, Hancock, and Brown [11] completed seminal ductile fracture experiments that the Johnson-Cook model was empirically motivated by. The key result obtained from the ductile fracture experiments was that the equivalent plastic strain at fracture decreases exponentially with increasing stress triaxiality. This result and Bridgman's analysis of the stress state at the necking localization are consistent with the analytical microvoid models of McClintock [2] and Rice and Tracey [3].

To experimentally investigate the effect of stress triaxiality on ductility over a broader range of stress states, Refs. [12–17] build on the work of Hancock and Mackenzie [10, 11] by exploring different geometries and loading conditions. More recently, however, it has been conclusively shown, through experimental studies, that triaxiality alone cannot model the ductile fracture over the full range of potential stress states. Wierzbicki et al. [18] first addressed this limitation and was later confirmed by Barsoum and Faleskog [19] through experimental work. The experimental work showed that by supplementing triaxiality with the Lode parameter, a three-dimensional state of stress is what ductility (plastic strain at fracture) depends on. Barsoum and Faleskog [19], using scanning electron microscopy, observed different rupture mechanisms under different loading conditions: internal void shearing at low (compression-dominated) triaxialities and growth and internal necking of voids at high (tension-dominated) triaxialities. Recent work investigating the dual dependence of triaxiality and the Lode parameter, as well as recent ductile fracture models incorporating both, can be found in Refs. [20–34].

1.3 Research Opportunity

The three-dimensional state of stress (equivalent plastic strain at fracture as a function of stress triaxiality and Lode parameter) is known as the failure locus and is a key ingredient in many ductile fracture models. The failure locus is developed for individual metals using an extensive experimental program involving numerous specimen geometries and loadings, with each combination characterizing a discrete point on the failure locus in the three-dimensional space. Each discrete point is then stitched into a continuous three-dimensional surface using biharmonic spline interpolation. For each experiment in the program, a parallel finite-element simulation is used to extract the triaxiality, Lode parameter, and failure strains. Standard mechanical tests are generally used to populate the failure locus, but standard tests can only capture a limited window of stress states. This limited window potentially leaves important regions of the failure locus unpopulated. For instance, a significant body of previous research (e.g., Ref. [35]) suggests that fracture will not occur above a stress triaxiality of 0.33 (known as the "cut-off" value). However, recent ballistic impact simulations involving 12.7-mm-thick Ti-6Al-4V titanium alloy plates predicted very large positive (compressive) triaxialities in the vicinity of the adiabatic shear band [36]. Several other recent experiments in Refs. [24, 37–40] explore ductile fracture at positive triaxialities further call into question this previous "cut-off" value. These results not only suggest the potentially unanticipated importance of the positive triaxiality (compressive) region of Lode-triaxiality stress space, but also the need to experimentally revisit previous interpretations of the "cut-off" value of the triaxiality.

1.4 Objectives, Scope, and Novel Contributions

Toward that end, this thesis investigates the ductile fracture of 6.35-mm-thick and 12.7-mm-thick Ti-6Al-4V titanium plate under compressive stress states. Specifically, our experimental plan is designed to interrogate the quasi-static ductile fracture behavior of Ti-6Al-

4V plate under complex, highly triaxial, compression-dominated stress states. To achieve this, our testing program employs a series of cylindrical compression specimens with asymmetric features and/or geometric irregularities including vertical through-holes, 45-degree through-holes, horizontal through-holes, a 45-degree slot, and a spherical recess. This test series is intended to complement previous ductile fracture experiments performed on the same lot of 12.7-mm-thick Ti-6Al-4V plate stock. Stereo digital image correlation is used to measure surface displacements and compute full-field strains at and near the fracture location. The experimental results are coupled with numerical simulations in LS-DYNA to calculate the stress state evolution and fracture strain at the site of fracture initiation. Weighted-average triaxialities of 0.61, 0.72, and 0.81 are reported for the specimens with through-holes, placing these experiments among the most compression-dominated in the literature.

CHAPTER II

THIN-PLATE EXPERIMENTAL FRACTURE SERIES

2.1 Material, Experimental Plan, and Specimen Preparation

The material considered in this chapter is the titanium alloy Ti-6Al-4V, with vendor-reported chemical composition shown in Table 2.1. Prior to receipt, the 6.35-mm-thick plate was cast, rolled to thickness, and vacuum creep flattened at 788 °C for 6 h.

Table 2.1: Vendor-reported chemical composition of 6.35-mm-thick Ti-6Al-4V

Si	Mn	Mo	Ti	Al	V	Fe	Cu	C
0.02	< 0.01	0.02	BAL	5.91	4.02	0.20	< 0.01	.02

Our experimental plan is designed to interrogate the quasi-static ductile fracture behavior of the 6.35-mm-thick Ti-6Al-4V plate under compression-dominated stress states. To achieve this, our testing program employs a pair of cylindrical compression (CC) specimens with length-to-diameter ratios H/D = 1 and 0.5 (Fig. 2.1).

The specimens in Fig. 2.1 were initially extracted from the Ti-6Al-4V plate as rectangular blanks using wire electrical discharge machining (EDM), with their longitudinal axes (loading direction) aligned with the plate's rolling direction. The rectangular blanks were subsequently machined into circular cylinders on a CNC mill using a helical cutting path along the length of the specimen. The cylindrical specimens were then cut to length using a grinder. Global tolerances for major specimen dimensions (e.g., cylinder diameter and length) were $\pm$ 0.127 mm. A contact profilometer was used to confirm that arithmetic mean surface roughness (Ra) values were less than 0.8 μm (ISO roughness grade N6).

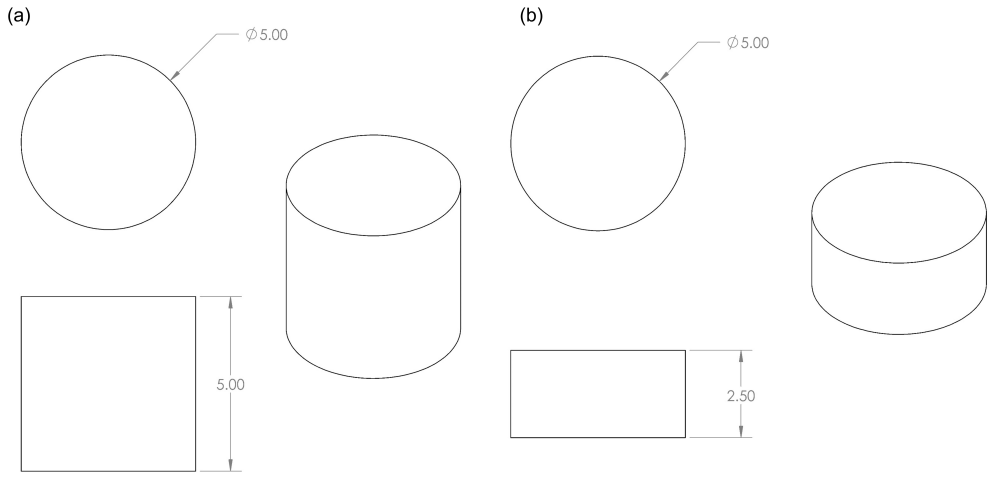

Figure 2.1: Cylindrical compression specimens with length-to diameter ratios (a) H/D = 1 and (b) H/D = 0.5.

2.2 Experimental Methods

2.2.1 Mechanical testing

Room-temperature quasi-static compression testing was performed on a servo-hydraulic load frame (MTS 793) under displacement control. Hydraulic wedge grips (MTS Series 647) fitted with custom tungsten carbide compression platens were used to axially compress the specimens during actuation. The test setup is shown in Fig. 2.2. Molybdenum disulfide grease (Molykote 106, DuPont) was used to lubricate the specimen-platen interfaces. During testing, specimens were compressed at a constant actuation speed of 0.306 mm/min (H/D = 1) or 0.138 mm/min (H/D = 0.5), which translates to a nominal strain rate of ~ 0.001 1/s in all cases. A 250-kN load cell (MTS 661.22H-01) was used to measure the axial load f in the specimens. An MTS FlexTest SE controller was used for both experimental

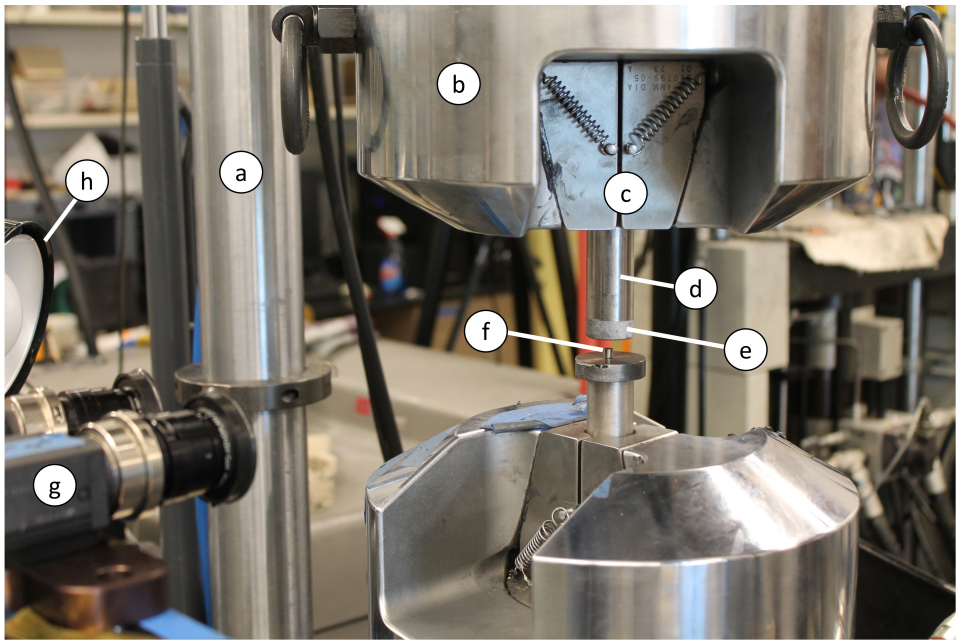

Figure 2.2: Compression test setup: (a) Servo-hydraulic load frame fixtured with (b) hydraulic wedge grips and (c) vee wedges that grip (d) steel push rods fitted with (e) tungsten carbide platens; (f) compression specimen, (g) stereo cameras, and (h) light source.

control and digital data acquisition. Each test was terminated manually after the specimen catastrophically fractured.

2.2.2 Digital image correlation

Stereo digital image correlation (DIC) was used to compute full-field surface displacements and strains during the deformation history of the specimens. In preparation for stereo DIC, a high-contrast black-on-white speckle pattern (feature size $\sim$ 4 px) was applied to each specimen using black spray-paint. Two high-performance digital cameras (Gazelle GZL-CL-41C6M-C, Point Grey Research) equipped with 105 mm lenses (AF Micro Nikkor f/2.8D, Nikon) captured the motion of the speckle pattern during testing at an acquisition rate of 1 Hz. The image resolution of the cameras is 2048 $\times$ 2048 px (4.2 MP). Additional

Table 2.2: DIC hardware and configuration parameters

Parameter	Test Series	
	H/D = 1	H/D = 0.5
Field of view (mm)	47.0 × 47.0	74.8 × 74.8
Image scale (μm/px)	22.95	36.50

DIC hardware parameters that varied from test to test are reported in Table 2.2. The calibration for each test series was accomplished with a 9 × 9 glass grid with a 3.0 mm pitch.

The images from each test were processed using commercial DIC software (VIC-3D 7, Correlated Solutions). All analyses used a direct correlation strategy, Gaussian subset weights, 90 percent center-weighted Gaussian strain filter weights, and optimized 6-tap spline interpolation. The subset size L_{sub}, step size L_{step}, and strain filter window L_{filt} (in px) – which varied from test to test – are reported in Table 2.3. The virtual strain gauge length (VSGL) L_{vsg} (in px) was then computed from these user-defined parameters using [41]:

$$L_{vsg} = (L_{filt} - 1)\, L_{step} + L_{sub} \tag{2.1}$$

The resulting VSGL was converted from discretized units (px) to physical units (mm) using the image scale, i.e., the calibrated physical length of each pixel (Table 2.2). The image scale depends on both the field of view and the camera sensor resolution.

The global axial displacement d is reported as the relative axial separation between two gauge marks measured using a DIC virtual extensometer (VE). (Note that a positive value of d denotes decreasing axial distance between the two gauge marks, which are initially separated by the VE length reported in Table 2.4.) This approach removes machine

Table 2.3: DIC software and analysis parameters

Parameter	Test Series	
	H/D = 1	H/D = 0.5
Subset size, L_{sub} (px)	29	29
Step size, L_{step} (px)	1	1
Strain filter window, L_{filt} (-)	5	5
VSGL, L_{vsg} (px)	33	33
VSGL, L_{vsg} (mm)	0.757	1.205

Table 2.4: DIC displacement and strain extraction

Test Series	VE Length (mm)	Strain Extraction
H/D = 1	2.199	$\sim 2.5 \times 4.7$ mm AOI
H/D = 0.5	0.763	$\sim 1.8 \times 4.0$ mm AOI

compliance from the measurement and thus provides more reliable axial displacement data than the servo-hydraulic load frame's integrated LVDT. For both test series, we report averaged values of the principal Hencky (true) strains e_1 and e_2 over areas of interest (AOIs) whose footprints enclose critical locations (e.g., strain localizations and/or potential fracture initiation sites) on the specimen surface; see Table 2.4.

2.3 Finite Element Analysis

Each test series in Fig. 2.1 was simulated using the finite element analysis (FEA) software LS-DYNA. This allows for measured data from the experiments to be compared to the corresponding results from a parallel numerical simulation. Agreement between the measured data and the simulation suggests that the simulation is accurately capturing the three-dimensional stresses and strains in the specimen. With agreement, the three-dimensional

stress and strain histories – which cannot be directly measured – can be extracted from the simulation. Of particular interest are the triaxiality, Lode parameter, and equivalent plastic strain histories at the location of fracture initiation, with the latter inferred from DIC images and post-mortem specimen inspection.

2.3.1 Triaxiality and Lode parameter

Common models for the ductile fracture of polycrystalline metals and alloys include the extended Mohr-Coulomb model [22] and the Hosford-Coulomb model [27]. These models generally employ an uncoupled damage indicator D, which increases with accumulated plastic strain. The damage increment ΔD accrued at each time step is the equivalent plastic strain increment normalized by the equivalent plastic strain at fracture $\bar{e}_f^p$, which depends on the triaxiality T and Lode parameter L, two parameters that characterize the three-dimensional state of stress. We adopt the following definitions for the triaxiality and Lode parameter:

$$T = -\frac{\sigma_m}{\bar{\sigma}_{vm}}, \qquad L = \frac{27}{2}\frac{J_3}{\bar{\sigma}_{vm}^3} \tag{2.2}$$

The mean stress σ_m and von Mises equivalent stress $\bar{\sigma}_{vm}$ in Eq. (2.2) can be calculated using

$$\sigma_m = \frac{I_1}{3}, \qquad \bar{\sigma}_{vm} = \sqrt{3J_2}\,, \tag{2.3}$$

with $I_1 = \operatorname{tr}\boldsymbol{\sigma}$ the first invariant of the Cauchy stress tensor $\boldsymbol{\sigma}$, and $J_2 = \frac{1}{2}\mathbf{S}\cdot\mathbf{S}$ and $J_3 = \det\mathbf{S}$ the second and third invariants of the deviatoric stress tensor $\mathbf{S} = \boldsymbol{\sigma} - \sigma_m\mathbf{I}$. Note that our definition of triaxiality (the one used in LS-DYNA) differs from the definition typically used in the literature by a negative sign. For example, with our definition, the stress triaxiality is 0.33 in a uniaxial compression test and -0.33 in a uniaxial tension test.

2.3.2 Simulation details

Table 2.5: Finite element mesh details

Test Series	Number of Elements	Characteristic Mesh Size (mm)	
		Near Features	Far from Features
CC H/D = 1	123,240	0.10	0.10
CC H/D = 0.5	65,960	0.10	0.10

Finite element simulations of the experiments (Fig. 2.1) were performed using explicit analyses in LS-DYNA (R12.1.0, Ansys). All meshes (Fig. 2.3, right) consisted of eight-node solid hexahedral elements with reduced integration, and varied in size and density from specimen to specimen (Table 2.5). Each individual specimen in this test series was modeled using as-machined dimensions in order to accurately simulate each test. To account for the tendency of under-integrated elements to hourglass, stiffness-based hourglass control (IHQ = 6) was employed with the default hourglass coefficient (QH = 0.1).

The two tungsten carbide compression platens were modeled as non-deformable rigid bodies. The response of the Ti-6Al-4V compression specimens was modeled using a publicly available elastic-plastic constitutive model (MAT-224-GYS) calibrated to 6.35-mm-thick Ti-6Al-4V coupon data [42,43]. Pre-yield response was modeled using isotropic linear elasticity, with Young's modulus $E = 110$ GPa and Poisson's ratio $\nu = 0.342$. Iso-rate post-yield response (0.001 1/s) was modeled using tabulated hardening curves (Fig. 2.3, left) from tension and compression tests performed in Ref. [43] with coupons extracted from the rolling direction of the plate.

The motion of the platens was restricted using the center of mass constraint option (CMO = 1). For the fixed platen, all translational and rotational degrees of freedom were constrained (CON1 = CON2 = 7). For the actuated platen, only axial translation was

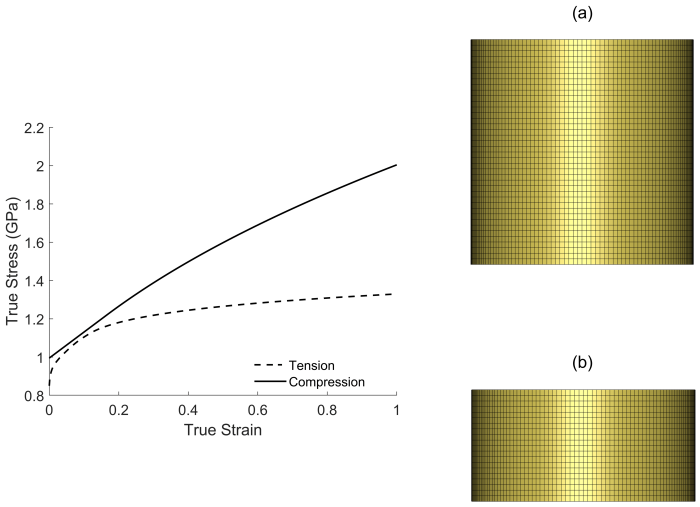

Figure 2.3: Left: User-defined hardening curve used in the numerical simulations. Right: Meshed monolithic cylindrical compression (CC) specimens with (a) H/D = 1 and (b) H/D = 0.5.

permitted at a constant speed of 0.3 m/s, with all other degrees of freedom constrained (CON1 = 6, CON2 = 7). Note that the loading speed (0.3 m/s) used in the simulations is significantly higher than the actuation speed employed in the experiments (cf. Section 2.3.1) to enable explicit analysis and reduce computational expense. This use of an "artificial" loading speed is enabled by a rate-independent plasticity model and confirming the absence of dynamic effects (and thus loading-speed dependence) in the numerical simulations [44]. For the latter, simulations were run over a wide range of "artificial" loading speeds (e.g., 1 m/s, 0.5 m/s, 0.3 m/s, 0.1 m/s) to confirm loading-speed independence and the absence of dynamic effects, and 0.3 m/s was found to be the largest acceptable actuation speed.

Contact at the specimen-platen interfaces was modeled using a built-in two-way penalty-based algorithm with segment-based searching (AUTOMATIC-SURFACE-TO-SURFACE).

The algorithm searched for both surface penetrations and edge-to-edge penetrations (DEPTH = 25). Contact stiffness was calculated based on stability considerations (SOFT = 1). Viscous damping was increased to 20% to damp oscillations normal to the contact surfaces. The static and dynamic coefficients of friction were set to 0.03 and 0.01 to match simulated and experimental barreling profiles. All other contact settings remained at their default value.

2.4 Results

In this section, we compare measured data – namely, force-displacement (f vs. d) response, and principal Hencky (true) strain histories (e_1 and e_2 vs. d) – from each test in our experimental program with the corresponding results from a parallel numerical simulation. Agreement between the measured data and the simulation suggests that the simulation is accurately capturing the three-dimensional stresses and strains in the specimen. With agreement, the three-dimensional stress and strain histories – which cannot be directly measured – are extracted from the simulation at the location of fracture initiation, which is inferred from DIC images and post-mortem specimen inspection.

Figures 2.4 and 2.5 compare experimental (DIC) and numerical (FEA) contour plots of the local axial strain on the surface of the specimen at different values of global compression $\Delta H/H$, where H is the length of the undeformed specimen and ΔH is the displacement of the actuated platen (which, in general, differs from the displacement d measured by the virtual extensometer). The bottom contour correlates to the DIC frame immediately prior to fracture initiation. The DIC strain field evolves from nearly homogeneous and axisymmetric at $\sim$ 20% compression to strongly heterogeneous and non-axisymmetric at $\sim$ 40% compression, with significant regions of localization. The simulations are unable

to capture this heterogeneity and circumferential variation in the axial strain field, and thus exhibit worsening agreement with increasing global compression. The heterogeneity and circumferential variation are more pronounced in the specimen with a lower length-to-diameter ratio (H/D = 0.5).

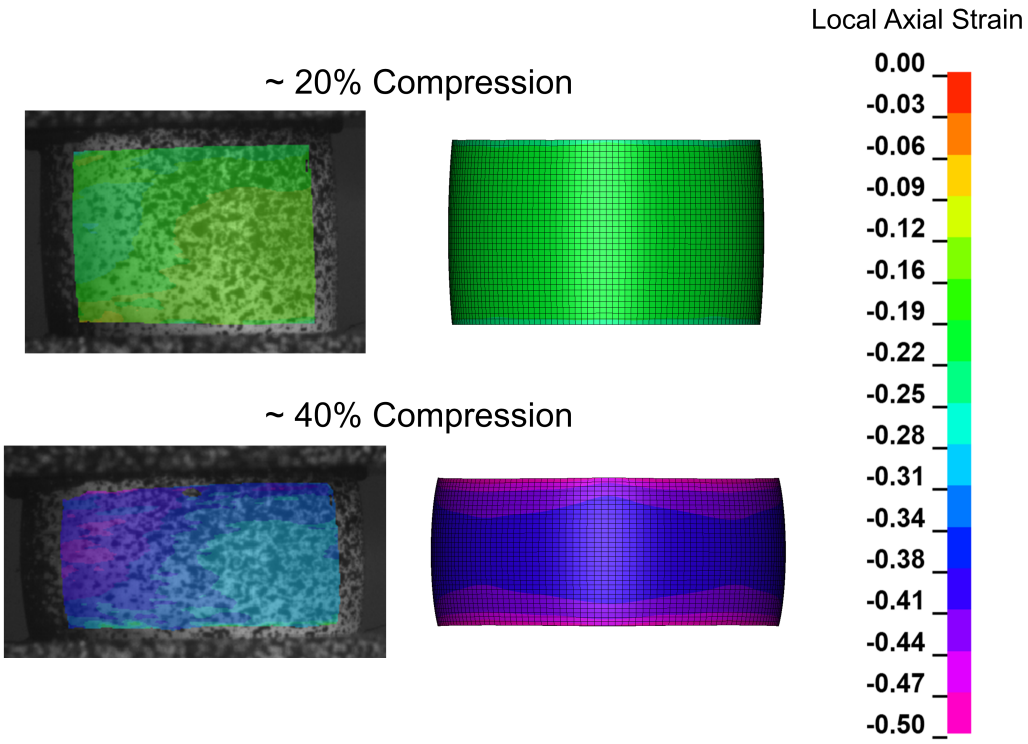

Figure 2.4: Local axial strain contours at ∼ 20% (top) and ∼ 40% (bottom) global compression from DIC (left) and FEA (right) for CC specimen with H/D = 1.

Figures 2.6 and 2.7 show the force-displacement curves, as well as the maximum and minimum principal strain histories, for the cylindrical compression specimens with aspect ratios H/D = 1 and 0.5, respectively. The experimental results show good repeatability (Figs. A.1 and A.2); thus, results for test N1 alone are shown here. The DIC principal strains are averaged over an area of interest on the specimen surface (Table 2.4). The FEA

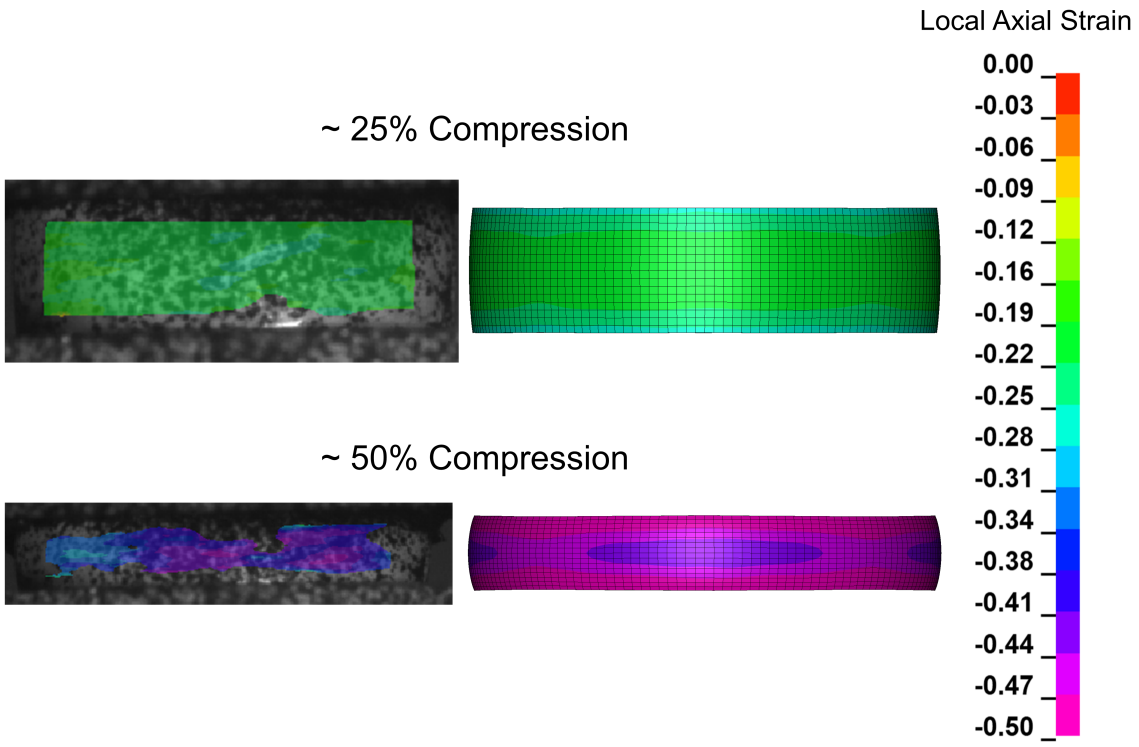

Figure 2.5: Local axial strain contours at $\sim$ 25% (top) and $\sim$ 50% (bottom) global compression from DIC (left) and FEA (right) for CC specimen with H/D = 0.5.

principal strains are averaged over a vertical strip of elements bounded at top and bottom by the footprint of the corresponding DIC AOI. (A vertical strip is used rather than a rectangular area since the simulation is axisymmetric.) Agreement in force-displacement response is very good for H/D = 1 and excellent for H/D = 0.5, with the simulation modestly over-predicting force in the former. Agreement in principal strain histories is excellent for H/D = 1 and very good for H/D = 0.5, with the simulation modestly over-predicting minimum principal strain in the latter, particularly at large axial displacements. This discrepancy is attributed to the simulation's inability to capture the strain heterogeneity and absence of axisymmetry observed in the experiments.

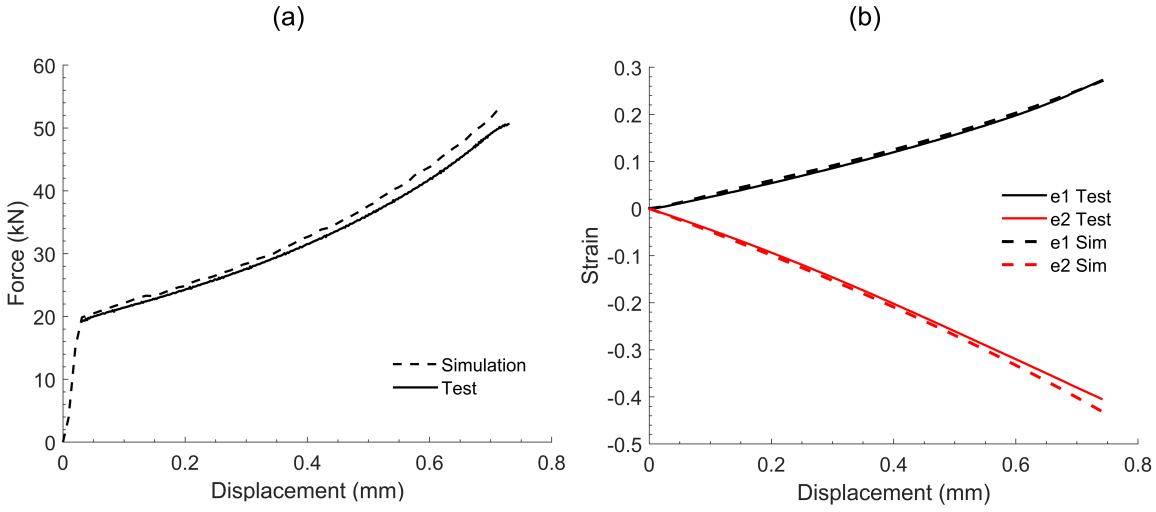

Figure 2.6: Comparison of experimental (measured) and numerical (simulated) (a) force-displacement response and (b) principal strain histories for CC specimen with H/D = 1 for test N1.

With sufficient agreement between the measured experimental data and the corresponding simulation results, the stress state (triaxiality T and Lode parameter L) and equivalent plastic strain ($\bar{e}^p$) histories can be extracted from the numerical simulations at the location of fracture initiation. This is inferred from DIC images and post-mortem specimen inspection. However, there is inherent uncertainty in identifying the precise location of fracture initiation, and in particular, whether a fracture event initiated on the surface or interior of the specimen. To address this uncertainty, we report stress state histories at the geometric center and free surface of the cylindrical compression specimen's horizontal mid-plane (Fig. 2.8 for H/D = 1 and Fig. 2.9 for H/D = 0.5), where fracture initiation seemingly occurred. These locations on the mid-plane constitute an upper and lower bound, respectively, on the stress state, which varies nearly linearly (not shown) between the geometric center and free

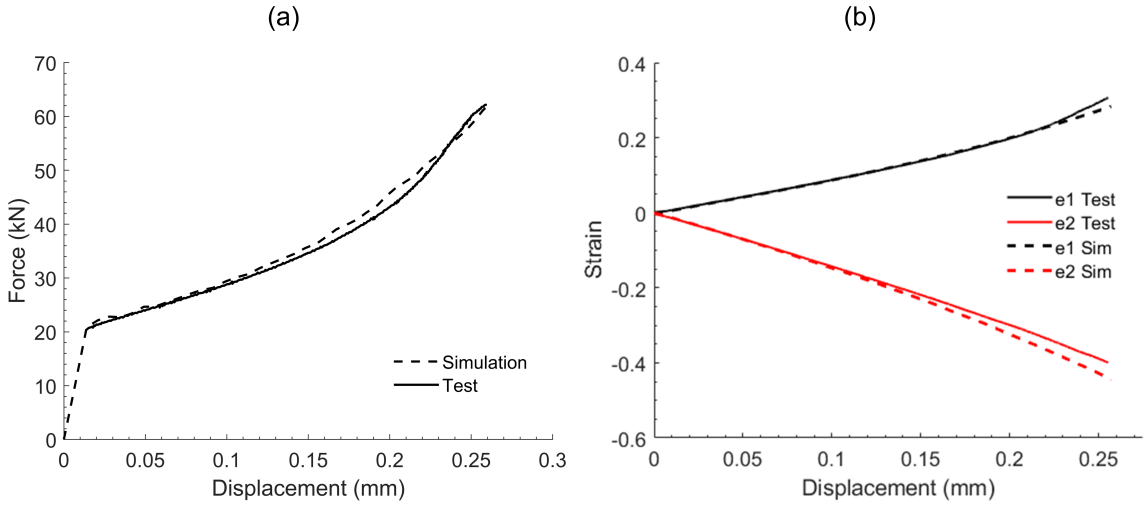

Figure 2.7: Comparison of experimental (measured) and numerical (simulated) (a) force-displacement response and (b) principal strain histories for CC specimen with H/D = 0.5 for test N1.

surface along the mid-plane. For both specimens (H/D = 1 and H/D = 0.5), the loading is nearly proportional (i.e., triaxiality and Lode parameter vary only minimally with plastic strain accumulation) at both the free surface and geometric center.

Weighted averages of the triaxiality and Lode parameter are calculated for each test between the onset of plastic deformation and fracture initiation:

$$T_{avg} = \frac{1}{\bar{e}_f^p} \int_0^{\bar{e}_f^p} T \, d\bar{e}^p \,, \qquad L_{avg} = \frac{1}{\bar{e}_f^p} \int_0^{\bar{e}_f^p} L \, d\bar{e}^p \tag{2.4}$$

Tables 2.6 and 2.7 report weighted averages of the triaxiality T_{avg} and Lode parameter L_{avg} for all of the tested cylindrical compression specimens. Also reported in Tables 2.6 and 2.7 is the equivalent plastic strain (EPS) at fracture $\bar{e}_f^p$ for each test. Table 2.8 reports the arithmetic mean of the weighted averages (mean $\pm$ one standard deviation) for each test

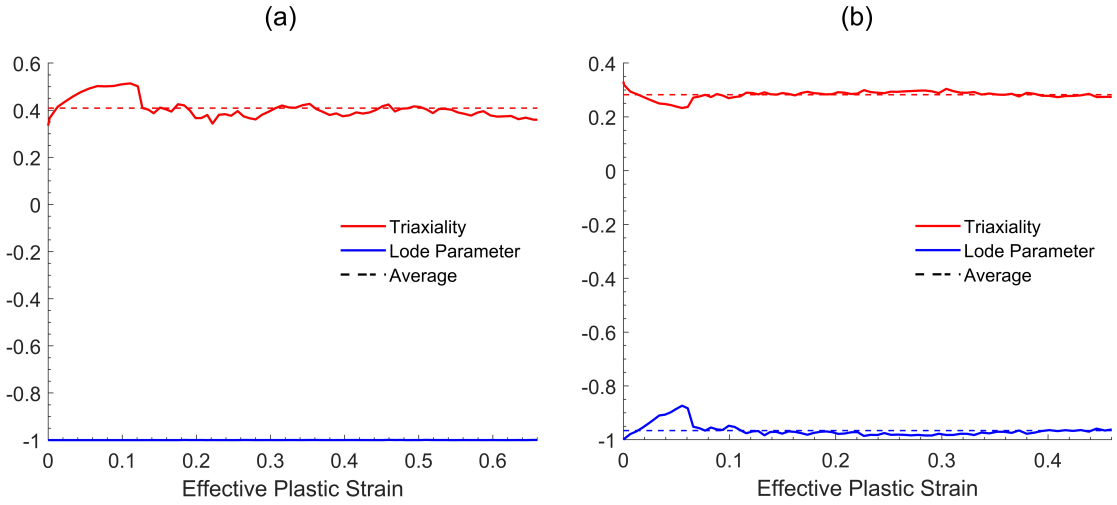

Figure 2.8: Evolution of stress state parameters with accumulated plastic strain at the (a) geometric center and (b) free surface of the CC specimen with H/D = 1.

series. The EPS at fracture is significantly higher at the center of the specimens than at the free surface, which suggests a higher likelihood of fracture initiation in that location. At the geometric center, both test series give a Lode parameter of -1.0; the triaxiality is modestly higher in the shorter specimens (0.48 vs. 0.41), although both stress states are highly compressive. The equivalent plastic strain at fracture is nominally lower in the shorter specimens (50% vs. 55%). Standard deviations are modest, indicative of good repeatability.

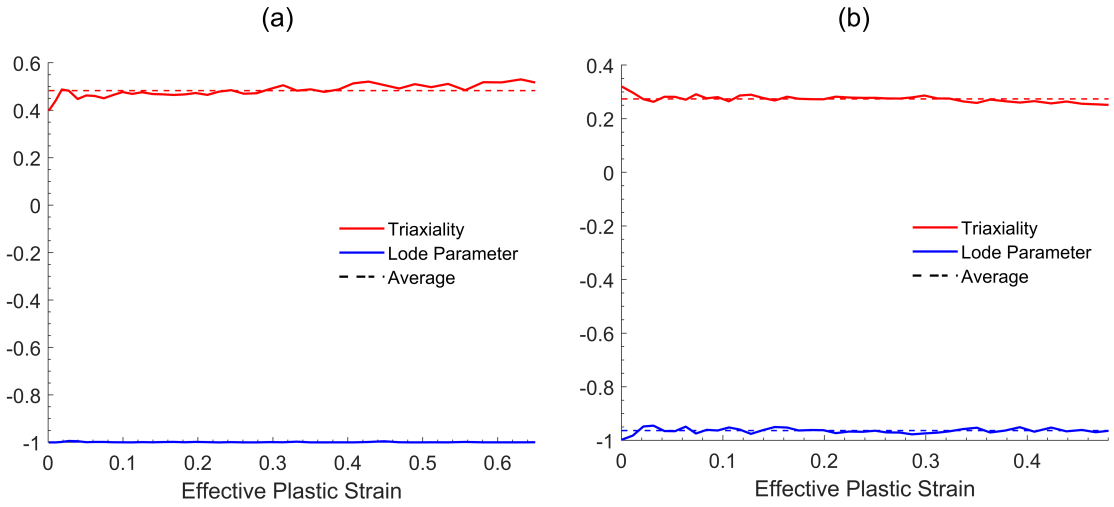

Figure 2.9: Evolution of stress state parameters with accumulated plastic strain at the (a) geometric center and (b) free surface of the CC specimen with H/D = 0.5.

Table 2.6: Weighted-average triaxiality, Lode parameter, and equivalent plastic strain at fracture for CC specimen with H/D = 1

Test Number		Triaxiality	Lode Parameter	EPS @ Fracture
Test N1	Upper	0.41	-1.0	0.65
	Lower	0.28	-0.97	0.45
Test N2	Upper	0.41	-1.0	0.52
	Lower	0.28	-0.97	0.34
Test N3	Upper	0.42	-1.0	0.49
	Lower	0.28	-0.96	0.32

Table 2.7: Weighted-average triaxiality, Lode parameter, and equivalent plastic strain at fracture for CC specimen with H/D = 0.5

Test Number		Triaxiality	Lode Parameter	EPS @ Fracture
Test N1	Center	0.48	-1.0	0.63
	Surface	0.27	-0.96	0.47
Test N2	Center	0.47	-1.0	0.43
	Surface	0.28	-0.96	0.34
Test N3	Center	0.47	-1.0	0.43
	Surface	0.28	-0.96	0.34

Table 2.8: Means for each test series

Test Series		Triaxiality	Lode Parameter	EPS @ Fracture
H/D = 1	Center	0.41 ± 0.0033	-1.00 ± 0.0001	0.55 ± 0.0818
	Surface	0.28 ± 0.0004	-0.97 ± 0.0012	0.37 ± 0.0657
H/D = 0.5	Center	0.48 ± 0.0072	-1.00 ± 0.0003	0.50 ± 0.1182
	Surface	0.28 ± 0.0028	-0.96 ± 0.0008	0.38 ± 0.0759

CHAPTER III

THICK-PLATE EXPERIMENTAL FRACTURE SERIES

3.1 Material, Experimental Plan, and Specimen Preparation

The material considered in this chapter is the titanium alloy Ti-6Al-4V, with vendor-reported chemical composition shown in Table 3.1. Prior to receipt, the 12.7-mm-thick plate was cast, rolled to thickness, and vacuum creep flattened at 760 °C for 8 h.

Table 3.1: Vendor-reported chemical composition of 12.7-mm-thick Ti-6Al-4V

N	C	Fe	O	H	Al	V	Y	Ti
0.006	0.016	0.18	0.17	0.0085	6.27	4.08	0.0004	BAL

Our experimental plan is designed to interrogate the quasi-static ductile fracture behavior of the 12.7-mm-thick Ti-6Al-4V plate under complex, highly triaxial, compression-dominated stress states. To achieve this, our testing program employs a series of cylindrical compression specimens with asymmetric features and/or geometric irregularities such as vertical through-holes (TH-V, Fig. B.1(b)), 45-degree through-holes (TH-45, Fig. B.1(c)), horizontal through-holes (TH-H, Fig. B.1(d)), a 45-degree slot (S-45, Fig. B.1(e)), and a spherical recess (SR, Fig. B.1(f)). These designs were adopted from Refs. [38, 39, 45]. Also included are standard cylindrical compression (CC) specimens with length-to-diameter ratios of H/D = 1 and 0.5 (Fig. B.1(a)). This test series is intended to complement previous ductile fracture experiments reported in Refs. [44, 46] on the same lot of 12.7-mm-thick Ti-6Al-4V plate stock; note that these previous tests typically interrogate Ti-6Al-4V under tension-dominated stress states, in contrast to the present work.

The specimens in Fig. B.1 were initially extracted from the Ti-6Al-4V plate as rectangular blanks using wire electrical discharge machining (EDM), with their longitudinal axes (loading direction) aligned with the plate's rolling direction. The rectangular blanks were subsequently machined into circular cylinders using a CNC mill with a helical cutting path along the length of the specimen. The specimens were then cut to length using a grinder. Through-holes (TH-V, TH-45, and TH-H) were bored using a CNC mill with a 0.5-mm drill attachment, while spherical recesses (SR) and 45-degree slots (S-45) were machined using wire EDM. Global tolerances for major specimen dimensions (e.g., cylinder diameter and length) were $\pm$ 0.127 mm, while local tolerances for fine features (e.g., through-hole diameters) were $\pm$ 0.0254 mm. A contact profilometer was used to confirm that arithmetic mean surface roughness (Ra) values were less than 0.8 μm (ISO roughness grade N6).

3.2 Experimental Methods

3.2.1 Mechanical testing

Room-temperature quasi-static compression testing was performed on a servo-hydraulic load frame (MTS 793) under displacement control. Hydraulic wedge grips (MTS Series 647) fitted with custom tungsten carbide compression platens were used to axially compress the specimens during actuation. The test setup is shown in Fig. 3.1. Molybdenum disulfide grease (Molykote 106, DuPont) was used to lubricate the specimen-platen interfaces. During testing, the specimens were compressed at differing actuation speeds (Table 3.2) to achieve a nominal strain rate of $\sim$ 0.001 1/s in each test. A 250-kN load cell (MTS 661.22H-01) was used to measure the axial load f in the specimens. (Note that in this thesis, a positive value of f implies a compressive load.) An MTS FlexTest SE controller was used for both experimental control and digital data acquisition. Each test was terminated manually

Table 3.2: Constant actuation speeds for each test series

Test Series	Actuation Speed (mm/min)
CC H/D = 1	0.34
CC H/D = 0.5	0.15
TH-V	0.72
TH-45	0.72
TH-H	0.72
S-45	0.90
SR	0.75

after the specimen catastrophically fractured. At least three tests were conducted for each specimen design.

3.2.2 Digital image correlation

Stereo digital image correlation (DIC) was used to compute full-field surface displacements and strains during the deformation history of the specimens. In preparation for stereo DIC, a high-contrast black-on-white speckle pattern (feature size $\sim$ 4 px) was applied to each specimen using black spray-paint. Two high-performance digital cameras (Gazelle GZL-CL-41C6M-C, Point Grey Research) equipped with 105 mm lenses (AF Micro Nikkor f/2.8D, Nikon) captured the motion of the speckle pattern during testing. The image resolution of the cameras is 2048 $\times$ 2048 px (4.2 MP). Additional DIC hardware parameters that varied from test to test are reported in Table 3.3. Independent calibrations for each test series were performed using a 9 $\times$ 9 glass grid with a 3.0 mm pitch.

The images from each test were processed using commercial DIC software (VIC-3D 7, Correlated Solutions). All analyses used a direct correlation strategy, Gaussian subset weights, 90 percent center-weighted Gaussian strain filter weights, and optimized 6-tap spline interpolation. The subset size L_{sub}, step size L_{step}, and strain filter window L_{filt}

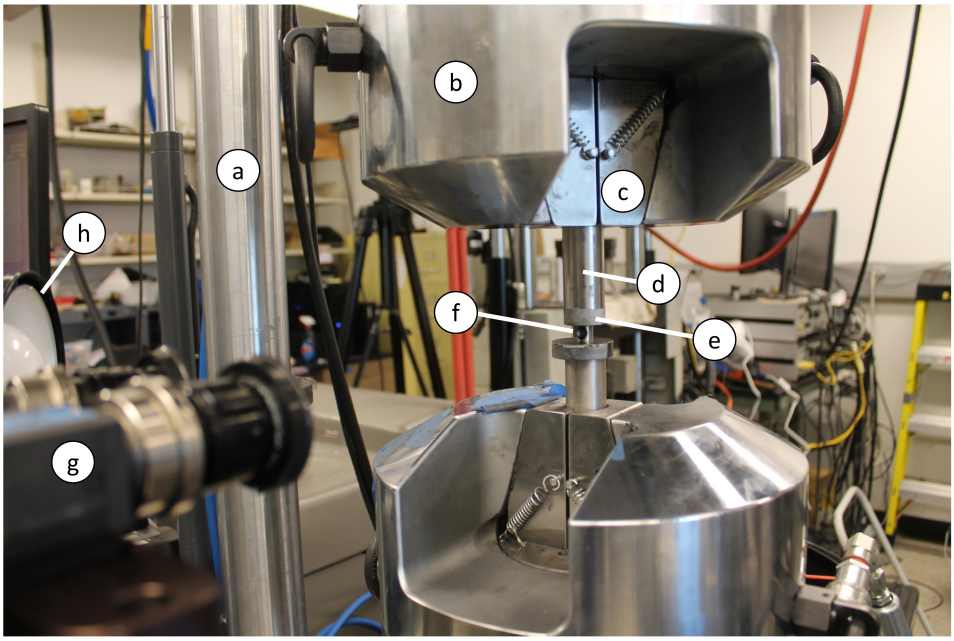

Figure 3.1: Compression test setup: (a) Servo-hydraulic load frame fixtured with (b) hydraulic wedge grips and (c) vee wedges that grip (d) steel push rods fitted with (e) tungsten carbide platens; (f) compression specimen, (g) stereo cameras, and (h) light source.

Table 3.3: DIC hardware and configuration parameters

Test Series	Field of View (mm)	Image Scale (μm/px)	Acquisition Rate (Hz)
CC	50.8 × 50.8	24.80	2
TH-V	37.3 × 37.3	18.23	1
TH-45	37.3 × 37.3	18.23	1
TH-H	37.3 × 37.3	18.23	1
S-45	50.8 × 50.8	24.80	1
SR	37.3 × 37.3	18.23	2

Table 3.4: DIC software and analysis parameters

Parameter	Test Series					
	CC	TH-V	TH-45	TH-H	S-45	SR
Subset size, L_{sub} (px)	31	35	35	35	33	35
Step size, L_{step} (px)	4	6	6	6	4	6
Strain filter window, L_{filt} (-)	5	5	5	5	5	5
VSGL, L_{vsg} (px)	47	59	59	59	49	59
VSGL, L_{vsg} (mm)	1.166	1.076	1.076	1.076	1.215	1.076

(in px) – which varied from test to test – are reported in Table 3.4. The virtual strain gauge length (VSGL) L_{vsg} (in px) was then computed from these user-defined parameters using [41]:

$$L_{vsg} = (L_{filt} - 1)\, L_{step} + L_{sub} \tag{3.1}$$

The resulting VSGL was converted from discretized units (px) to physical units (mm) using the image scale, i.e., the calibrated physical length of each pixel (Table 3.3). The image scale depends on both the field of view and the camera sensor resolution.

The global axial displacement d is reported as the relative axial separation between two gauge marks measured using a DIC virtual extensometer (VE). (Note that a positive value of d denotes decreasing axial distance between the two gauge marks, which are initially separated by the VE length reported in Table 3.5.) This approach removes machine compliance from the measurement and thus provides more reliable axial displacement data than the servo-hydraulic load frame's integrated LVDT. Strategies for extracting the principal Hencky (true) strains e_1 and e_2 on the specimen surface are summarized in Table 3.5. Specifically, the 45-degree slot (S-45) and the spherical recess (SR) test series report *point-wise* values of e_1 and e_2 from a virtual strain gauge placed at a *local* point of interest (e.g., strain localization and/or fracture initiation site) on the specimen surface. The cylindrical

Table 3.5: DIC displacement and strain extraction

Test Series	VE Length (mm)	Strain Extraction
CC H/D = 1	3.87	$\sim 4.2 \times 4.8$ mm AOI
CC H/D = 0.5	1.53	$\sim 2.4 \times 4.2$ mm AOI
TH-V	8.00	$\sim 7.7 \times 5.8$ mm AOI
TH-45	9.05	$\sim 7.0 \times 8.5$ mm AOI
TH-H	9.63	$\sim 8.1 \times 7.0$ mm AOI
S-45	12.6	VSG at fracture initiation location
SR	6.93	VSG at fracture initiation location

compression (CC) and all through-hole (TH-V, TH-45, TH-H) test series report averaged values of e_1 and e_2 over areas of interest (AOIs) whose footprints enclose critical locations (e.g., strain localizations and/or potential fracture initiation sites) on the specimen surface.

3.3 Finite Element Analysis

Each test series in Fig. B.1 was simulated using the finite element analysis (FEA) software LS-DYNA. This allows for measured data from the experiments to be compared to the corresponding results from a parallel numerical simulation. Agreement between the measured data and the simulation suggests that the simulation is accurately capturing the three-dimensional stresses and strains in the specimen. With agreement, the three-dimensional stress and strain histories – which cannot be directly measured – can be extracted from the simulation. Of particular interest are the triaxiality, Lode parameter, and equivalent plastic strain histories at the location of fracture initiation.

3.3.1 Triaxiality and Lode parameter

Common models for the ductile fracture of polycrystalline metals and alloys include the extended Mohr-Coulomb model [22] and the Hosford-Coulomb model [27]. These models

generally employ an uncoupled damage indicator D, which increases with accumulated plastic strain. The damage increment ΔD accrued at each time step is the equivalent plastic strain increment normalized by the equivalent plastic strain at fracture $\bar{e}_f^p$, which depends on the stress triaxiality T and Lode parameter L, two parameters that characterize the three-dimensional state of stress. We adopt the following definitions for the triaxiality and Lode parameter:

$$T = -\frac{\sigma_m}{\bar{\sigma}_{vm}}, \qquad L = \frac{27}{2}\frac{J_3}{\bar{\sigma}_{vm}^3} \tag{3.2}$$

The mean stress σ_m and von Mises equivalent stress $\bar{\sigma}_{vm}$ in Eq. (3.2) can be calculated using

$$\sigma_m = \frac{I_1}{3}, \qquad \bar{\sigma}_{vm} = \sqrt{3J_2}\,, \tag{3.3}$$

with $I_1 = \operatorname{tr}\boldsymbol{\sigma}$ the first invariant of the Cauchy stress tensor $\boldsymbol{\sigma}$, and $J_2 = \frac{1}{2}\mathbf{S}\cdot\mathbf{S}$ and $J_3 = \det\mathbf{S}$ the second and third invariants of the deviatoric stress tensor $\mathbf{S} = \boldsymbol{\sigma} - \sigma_m\mathbf{I}$. Note that our definition of triaxiality (the one used in LS-DYNA) differs from the definition typically used in the literature by a negative sign. For example, with our definition, the stress triaxiality is 0.33 in a uniaxial compression test and -0.33 in a uniaxial tension test.

3.3.2 Simulation details

Finite element simulations of the experiments (Fig. B.1) were performed using an explicit scheme in LS-DYNA (R12.1.0, Ansys) with massively parallel processing. All meshes (Fig. 3.2, right) consisted of eight-node solid hexahedral elements with reduced integration, and varied in size and density from specimen to specimen (Table 3.6). The complexity of the specimens in this test series made it difficult to get as-machined dimensions using conventional metrology techniques (e.g., digital calipers). Thus, the specimens with through-holes, spherical recesses, and 45-degree slots were simulated using their nominal (CAD) dimensions. The standard cylindrical compression specimens, which do not have complex internal

Table 3.6: Finite element mesh details

Test Series	Number of Elements	Characteristic Mesh Size (mm)	
		Near Features	Far from Features
CC H/D = 1	279,180	0.10	0.10
CC H/D = 0.5	144,000	0.10	0.10
TH-V	799,444	0.05	0.15
TH-45	976,456	0.05	0.15
TH-H	2,309,458	0.05	0.15
S-45	276,712	0.10	0.15
SR	417,723	0.10	0.15

features, were simulated using the as-machined dimensions for each specimen. To account for the tendency of under-integrated elements to hourglass, stiffness-based hourglass control (IHQ = 6) was employed with the default hourglass coefficient (QH = 0.1).

The response of the Ti-6Al-4V specimens was modeled using a custom elastic-plastic constitutive model with tension-compression yield differential (MAT-224-GYS) calibrated to 12.7-mm-thick Ti-6Al-4V coupon data [43]. Pre-yield response was modeled using isotropic linear elasticity, with Young's modulus $E = 110$ GPa and Poisson's ratio $\nu = 0.342$. Iso-rate post-yield response (0.001 1/s) was modeled using tabulated hardening curves (Fig. 3.2, left) from tension and compression tests performed in Ref. [43] with coupons extracted from the rolling direction of the plate.

The motion of the platens was restricted using the center of mass constraint option (CMO = 1). For the fixed platen, all translational and rotational degrees of freedom were constrained (CON1 = CON2 = 7). For the actuated platen, only axial translation at a constant speed of 0.3 m/s was permitted, with all other degrees of freedom constrained (CON1 = 6, CON2 = 7). Note that the loading speed (0.3 m/s) used in the simulations is

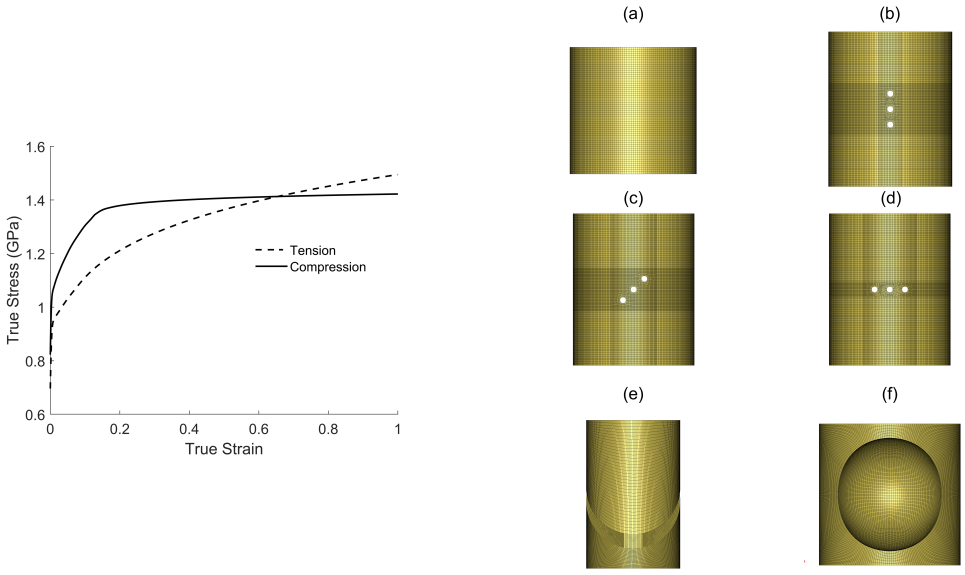

Figure 3.2: Left: User-defined hardening curve used in the numerical simulations. Right: Meshed cylindrical compression specimens with (a) monolithic geometry (CC), (b) vertical through-holes (TH-V), (c) 45-degree through-holes (TH-45), (d) horizontal through-holes (TH-H), (e) a 45-degree slot (S-45), and (f) a spherical recess (SR).

significantly higher than the actuation speed employed in the experiments (cf. Section 3.2.1) to enable explicit analysis and reduce computational expense. This use of an "artificial" loading speed is enabled by using a rate-independent constitutive model, and its veracity is confirmed by the absence of dynamic effects (and thus loading-speed dependence) in the numerical simulations [44]. For the latter, simulations were run over a wide range of "artificial" loading speeds (e.g., 1 m/s, 0.5 m/s, 0.3 m/s, 0.1 m/s) to confirm loading-speed independence and the absence of dynamic effects, and 0.3 m/s was found to be the largest acceptable actuation speed.

Contact at the specimen-platen interfaces was modeled using a built-in two-way penalty-based algorithm with segment-based searching (AUTOMATIC-SURFACE-TO-SURFACE). The algorithm searched for both surface penetrations and edge-to-edge penetrations (DEPTH

= 25). Contact stiffness was calculated based on stability considerations (SOFT = 1). Viscous damping was increased to 20% to damp oscillations normal to the contact surfaces. The static and dynamic coefficients of friction were set to 0.03 and 0.01 to match simulated and experimental barreling profiles. All other contact parameters remained at their default settings.

3.4 Results

In this section, we compare measured data – namely, force-displacement (f vs. d) response, and principal Hencky (true) strain histories (e_1 and e_2 vs. d) – from each test in our experimental program with the corresponding results from a parallel numerical simulation. Agreement between the measured data and the simulation suggests that the simulation is accurately capturing the three-dimensional stresses and strains in the specimen. With agreement, the three-dimensional stress and strain histories – which cannot be directly measured – are extracted from the simulation at the location of fracture initiation, which is inferred from DIC images and post-mortem specimen inspection.

3.4.1 Cylindrical compression (CC) specimens

In what follows, we compare measured experimental data with the corresponding results from parallel finite element simulations for cylindrical compression specimens with aspect ratios H/D = 1 and 0.5. Figures 3.3 and 3.4 compare experimental (DIC) and numerical (FEA) contour plots of the local axial strain on the surface of the specimen at different values of global compression $\Delta H/H$, where H is the length of the undeformed specimen and ΔH is the displacement of the actuated platen (which, in general, differs from the displacement d measured by the virtual extensometer). The bottom contour correlates to the DIC frame immediately prior to fracture initiation. The DIC strain field evolves from

nearly homogeneous and axisymmetric at $\sim$ 10% compression to strongly heterogeneous and non-axisymmetric at $\sim$ 20% compression, with significant regions of localization. The simulations are unable to capture this heterogeneity and circumferential variation in the axial strain field, and thus exhibit worsening agreement with increasing global compression. The heterogeneity and circumferential variation are more pronounced in the specimen with a lower length-to-diameter ratio (H/D = 0.5).

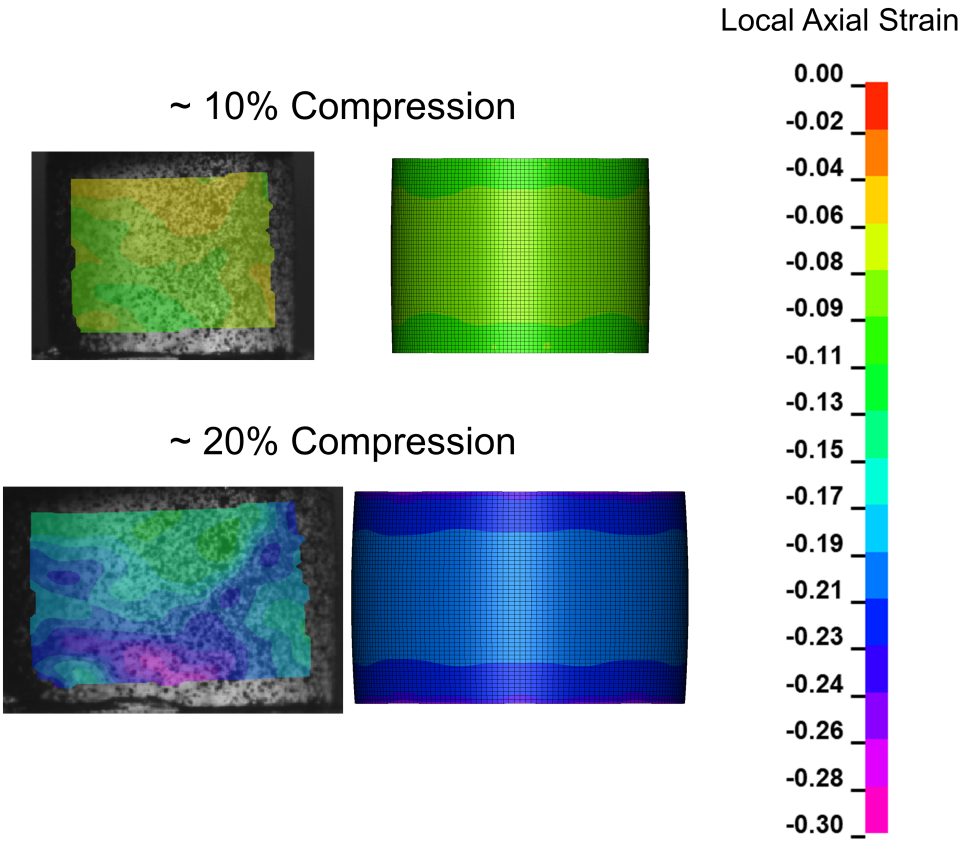

Figure 3.3: Local axial strain contours at $\sim$ 10% (top) and $\sim$ 20% (bottom) global compression from DIC (left) and FEA (right) for CC specimen with H/D = 1.

Figures 3.5 and 3.6 show the force-displacement curves, as well as the maximum and minimum principal strain histories, for the cylindrical compression specimens with aspect

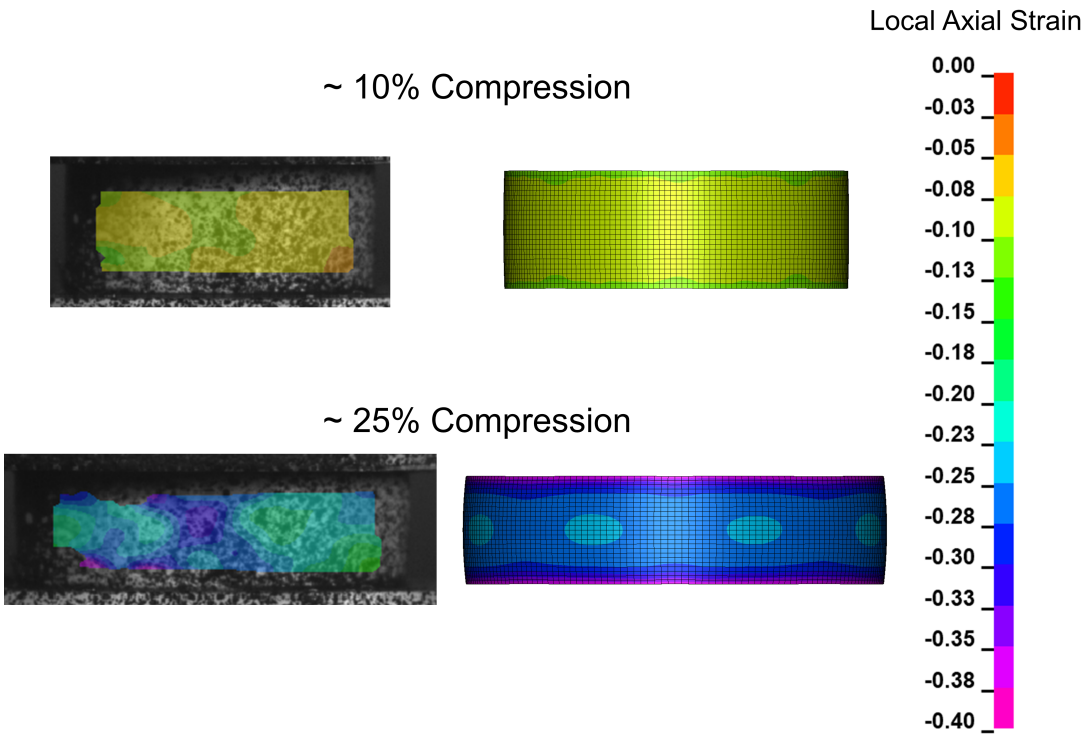

Figure 3.4: Local axial strain contours at $\sim$ 10% (top) and $\sim$ 25% (bottom) global compression from DIC (left) and FEA (right) for CC specimen with H/D = 0.5.

ratios H/D = 1 and 0.5, respectively. The experimental results show good repeatability (Figs. B.2 and B.3); thus, results for test N1 alone are shown here. The DIC principal strains are averaged over an area of interest on the specimen surface (Table 3.5). The FEA principal strains are averaged over a vertical strip of elements bounded at top and bottom by the footprint of the corresponding DIC AOI. (A vertical strip is used rather than a rectangular area since the simulation is axisymmetric.) Agreement in force-displacement response is excellent for H/D = 1 and good for H/D = 0.5, with the simulation over-predicting force in the latter. Agreement in principal strain histories is excellent for H/D = 1 and very good for H/D = 0.5, with the simulation over-predicting the minimum principal

strain in the latter. This discrepancy is attributed to the simulation's inability to capture the strain heterogeneity and absence of axisymmetry observed in the experiments.

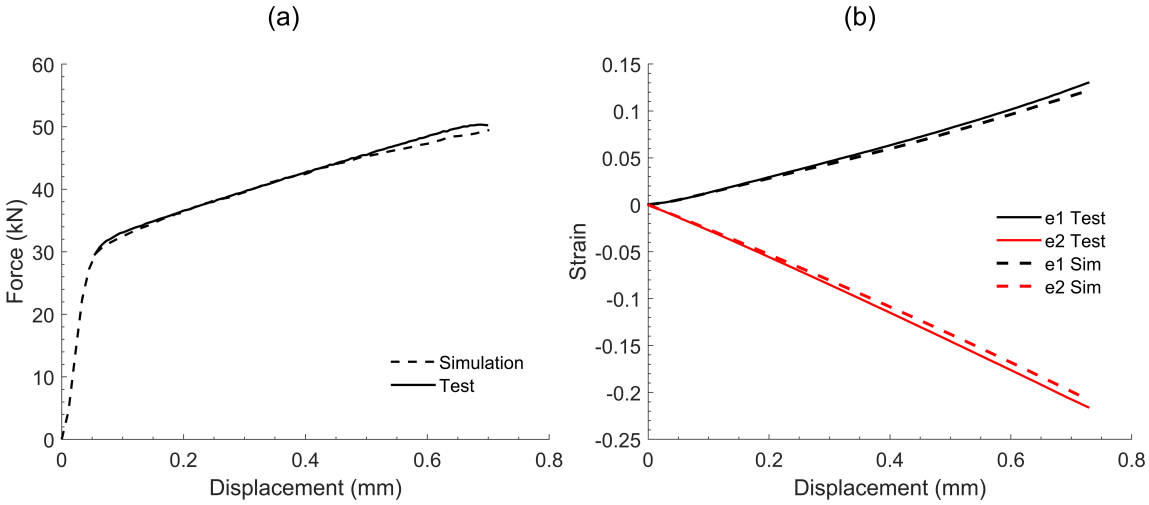

Figure 3.5: Comparison of experimental (measured) and numerical (simulated) (a) force-displacement response and (b) principal strain histories for CC specimen with H/D = 1 for test N1.

With sufficient agreement between the measured experimental data and the corresponding simulation results, the stress state (triaxiality T and Lode parameter L) and equivalent plastic strain ($\bar{e}^p$) histories can be extracted from the numerical simulations at the location of fracture initiation. This is inferred from DIC images and post-mortem specimen inspection. However, there is inherent uncertainty in identifying the precise location of fracture initiation, and in particular, whether a fracture event initiated on the surface or interior of the specimen. To address this uncertainty, we report stress state histories at the geometric center and free surface of the cylindrical compression specimen's horizontal mid-plane (Fig. 3.7 for H/D = 1 and Fig. 3.8 for H/D = 0.5), where fracture initiation seemingly occurred.

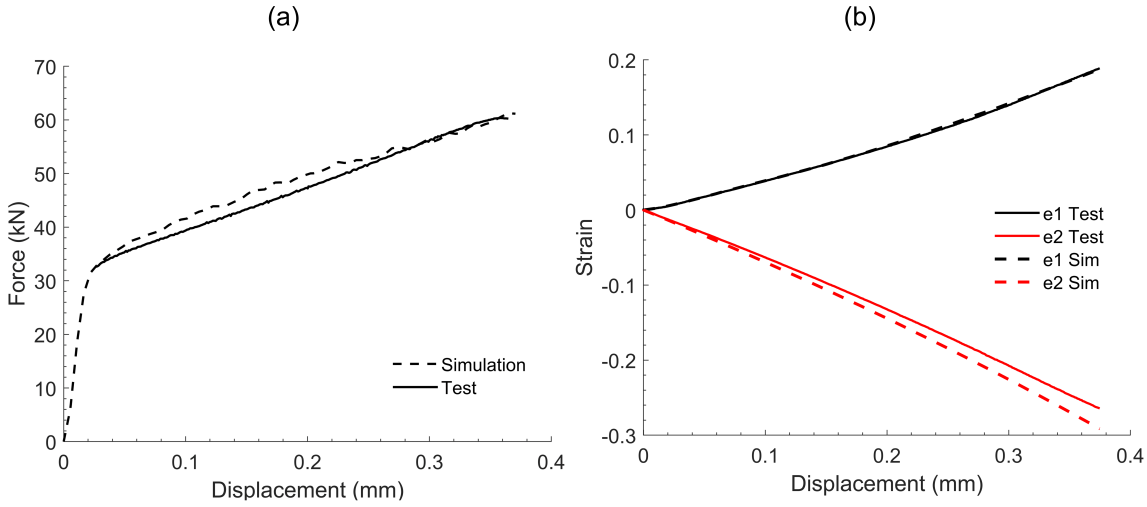

Figure 3.6: Comparison of experimental (measured) and numerical (simulated) (a) force-displacement response and (b) principal strain histories for CC specimen with H/D = 0.5 for test N1.

These locations on the mid-plane constitute an upper and lower bound, respectively, on the stress state, which varies nearly linearly (not shown) between the geometric center and free surface along the mid-plane. For both specimens (H/D = 1 and H/D = 0.5), the loading is nearly proportional at the free surface (i.e., triaxiality and Lode parameter vary only minimally with plastic strain accumulation). This also holds true at the geometric center of the shorter specimen (H/D = 0.5). In contrast, at the geometric center of the longer specimen (H/D = 1), the triaxiality increases nearly monotonically with plastic strain, although the Lode parameter exhibits negligible variation.

Weighted averages of the triaxiality and Lode parameter are calculated for each test between the onset of plastic deformation and fracture initiation:

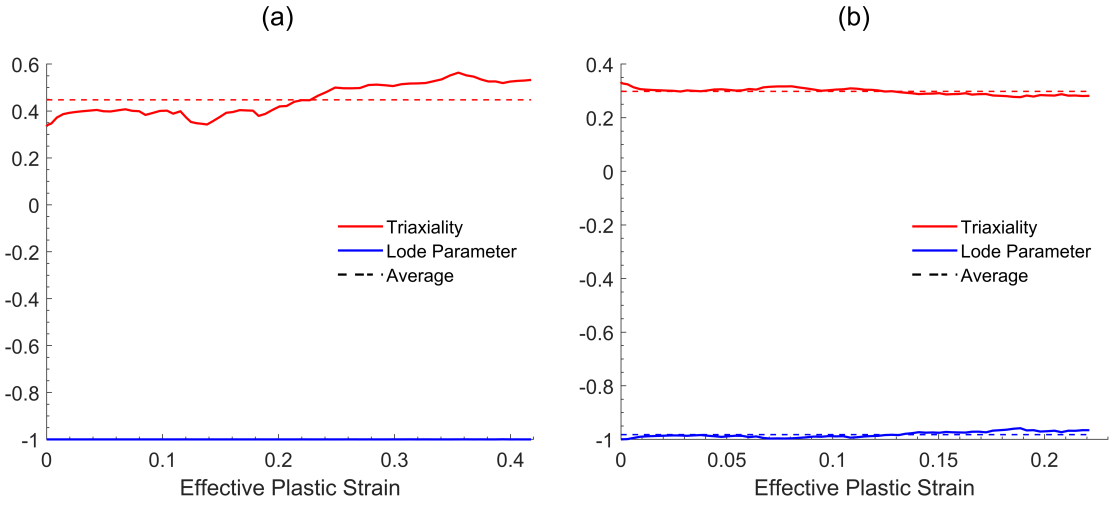

Figure 3.7: Evolution of stress state parameters with accumulated plastic strain at the (a) geometric center and (b) free surface of the CC specimen with H/D = 1 for test N1.

$$T_{avg} = \frac{1}{\bar{e}_f^p} \int_0^{\bar{e}_f^p} T \, d\bar{e}^p \,, \qquad L_{avg} = \frac{1}{\bar{e}_f^p} \int_0^{\bar{e}_f^p} L \, d\bar{e}^p \tag{3.4}$$

Tables 3.7 and 3.8 report weighted averages of the triaxiality T_{avg} and Lode parameter L_{avg} for all of the tested cylindrical compression specimens. Also reported in Tables 3.7 and 3.8 is the equivalent plastic strain (EPS) at fracture $\bar{e}_f^p$ for each test. Table 3.9 reports the arithmetic mean of the weighted averages (mean $\pm$ one standard deviation) for each test series. The EPS at fracture is significantly higher at the center of the specimens than at the free surface, which suggests a higher likelihood of fracture initiation in that location. At the geometric center, both test series give a Lode parameter of -1.0; the triaxiality is modestly higher in the shorter specimens (0.45 vs. 0.43), although both stress states are highly compressive. The equivalent plastic strain at fracture is nominally lower in the

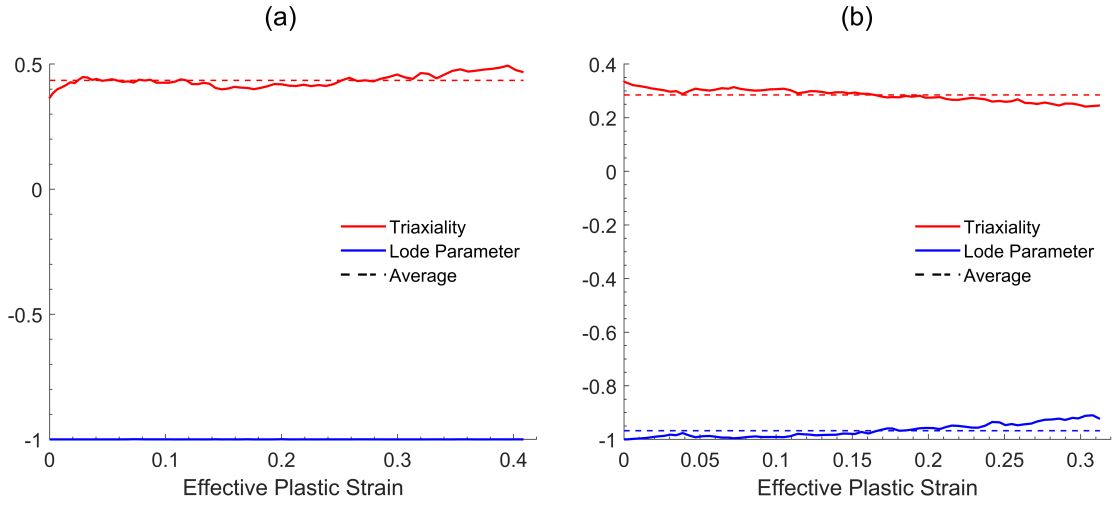

Figure 3.8: Evolution of stress state parameters with accumulated plastic strain at the (a) geometric center and (b) free surface of the CC specimen with H/D = 0.5 for test N1.

shorter specimens (33% vs. 44%). Standard deviations are modest, indicative of good repeatability.

3.4.2 Specimens with vertical through-holes (TH-V)

In what follows, we compare measured experimental data with the corresponding results from parallel finite element simulations for cylindrical compression specimens with vertical through-holes (TH-V). Figure 3.9 compares experimental (DIC) and numerical (FEA) contour plots of the local axial strain on the surface of the specimen at different values of global compression $\Delta H/H$, where H is the length of the undeformed specimen and ΔH is the displacement of the actuated platen (which, in general, differs from the displacement d measured by the virtual extensometer). The bottom contour correlates to the DIC frame immediately prior to fracture initiation. The DIC strain field evolves from nearly homogeneous

Table 3.7: Weighted-average triaxiality, Lode parameter, and equivalent plastic strain at fracture for CC specimen with H/D = 1

Test Number		Triaxiality	Lode Parameter	EPS @ Fracture
Test N1	Center	0.45	-1.00	0.41
	Surface	0.30	-0.98	0.22
Test N2	Center	0.45	-1.00	0.46
	Surface	0.30	-0.98	0.25
Test N3	Center	0.46	-1.00	0.46
	Surface	0.30	-0.98	0.24

Table 3.8: Weighted-average triaxiality, Lode parameter, and equivalent plastic strain at fracture for CC specimen with H/D = 0.5

Test Number		Triaxiality	Lode Parameter	EPS @ Fracture
Test N1	Center	0.44	-1.00	0.40
	Surface	0.29	-0.97	0.31
Test N2	Center	0.43	-1.00	0.30
	Surface	0.29	-0.97	0.25
Test N3	Center	0.42	-1.00	0.30
	Surface	0.29	-0.98	0.24

Table 3.9: Means for each test series

Test Series		Triaxiality	Lode Parameter	EPS @ Fracture
H/D = 1	Center	0.45 ± 0.0040	-1.00 ± 0.0001	0.44 ± 0.0311
	Surface	0.30 ± 0.0014	-0.98 ± 0.0011	0.24 ± 0.0176
H/D = 0.5	Center	0.43 ± 0.0069	-1.00 ± 0.0002	0.33 ± 0.0591
	Surface	0.29 ± 0.0042	-0.97 ± 0.0050	0.27 ± 0.0366

and axisymmetric at $\sim 5\%$ compression to strongly heterogeneous and non-axisymmetric at $\sim 10\%$ compression, with significant regions of localization. The simulations are unable to capture this heterogeneity and circumferential variation in the axial strain field, and thus exhibit worsening agreement with increasing global compression. However, the simulation does capture the localization around the through-holes.

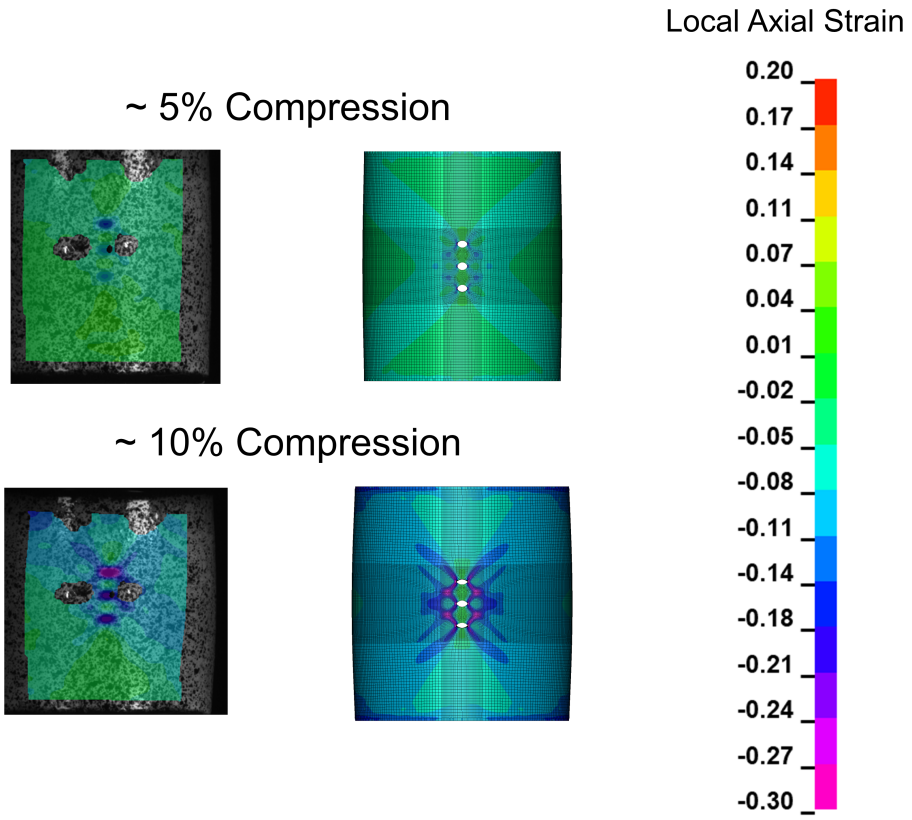

Figure 3.9: Local axial strain contours at $\sim 5\%$ (top) and $\sim 10\%$ (bottom) global compression from DIC (left) and FEA (right) for TH-V.

Figure 3.10 shows the force-displacement curves, as well as the maximum and minimum principal strain histories, for the cylindrical compression specimens with vertical through-holes (TH-V). The DIC principal strains are averaged over an area of interest on the spec-

imen surface (Table 3.5). The FEA principal strains are averaged over a rectangular area of elements bounded by the footprint of the corresponding DIC AOI. Agreement in force-displacement response is good for TH-V, with the simulation over-predicting force slightly in a couple tests. Agreement in principal strain histories is excellent, with the simulation falling within all tests curves.

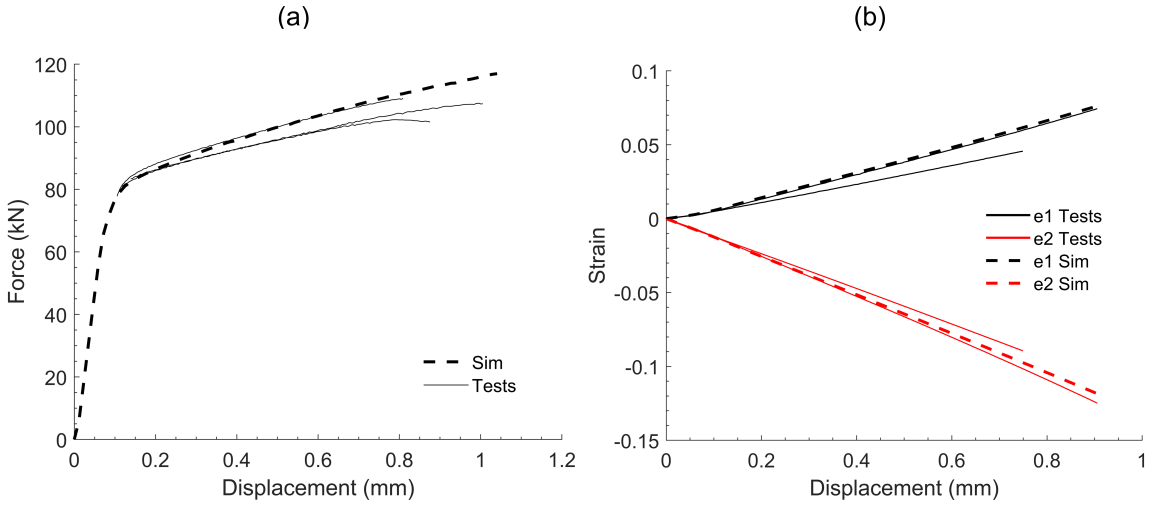

Figure 3.10: Comparison of experimental (measured) and numerical (simulated) (a) force-displacement response and (b) principal strain histories for TH-V specimen.

With sufficient agreement between the measured experimental data and the corresponding simulation results, the stress state (triaxiality T and Lode parameter L) and equivalent plastic strain ($\bar{e}^p$) histories can be extracted from the numerical simulations at the location of fracture initiation. This is inferred from DIC images and post-mortem specimen inspection. However, there is inherent uncertainty in identifying the precise location of fracture initiation, and in particular, whether a fracture event initiated on the surface or interior of

the specimen. To address this uncertainty, we report stress state histories at the geometric center and free surface of the cylindrical compression specimen with vertical through-holes (TH-V). The fracture location for TH-V appears to be at the mid-hole on the sides (Fig. 3.11). These locations on the mid-hole constitute an upper and lower bound, respectively, on the stress state, which varies nearly linearly (not shown) between the geometric center and free surface. For TH-V specimens, the loading increases nearly linearly at the free surface (i.e., triaxiality and Lode parameter increase linearly with plastic strain accumulation). This also holds true at the geometric center of the specimen.

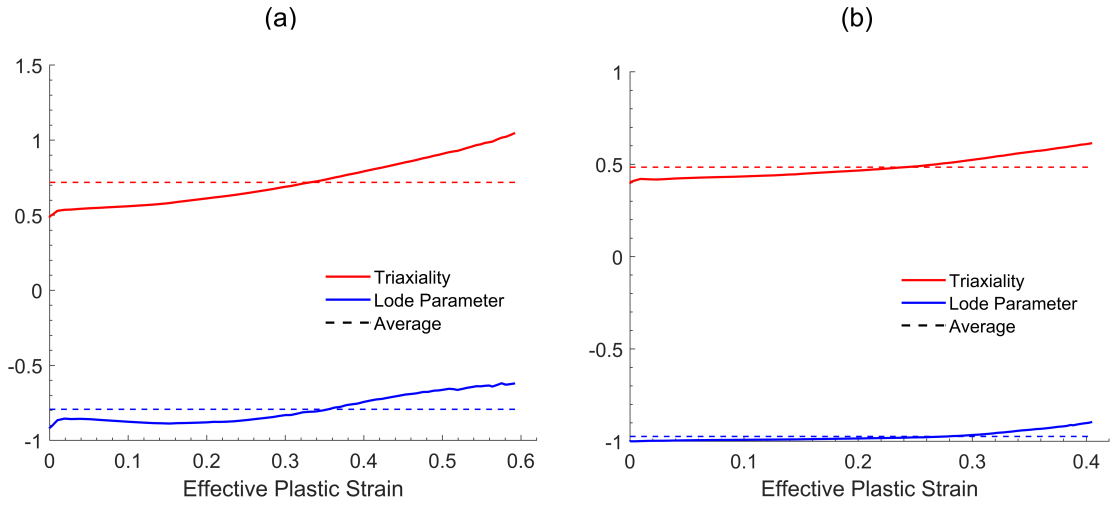

Figure 3.11: Evolution of stress state parameters with accumulated plastic strain at the (a) geometric center and (b) free surface of the TH-V specimen.

Weighted averages of the triaxiality and Lode parameter are calculated for each test between the onset of plastic deformation and fracture initiation using Eq. 3.4. Table 3.10 reports the weighted average of the triaxiality T_{avg} and Lode parameter L_{avg} for cylindri-

cal compression specimen with vertical through-holes. Also reported in Table 3.10 is the equivalent plastic strain (EPS) at fracture $\bar{e}_f^p$. The EPS at fracture is slightly higher at the center of the specimens than at the free surface, which suggests a higher likelihood of fracture initiation in that location. At the geometric center, TH-V gives a Lode parameter of -0.79, while the free edge gives a Lode parameter of -0.97; the triaxiality is significantly higher in the geometric center of the specimen (0.72 vs. 0.48), although both stress states are highly compressive. The equivalent plastic strain at fracture is much lower on the free edge of the specimen (41% vs. 59%).

Table 3.10: Weighted-average triaxiality, Lode parameter, and equivalent plastic strain at fracture for TH-V specimen

Specimen		Triaxiality	Lode Parameter	EPS @ Fracture
TH-V	Center	0.72	-0.79	0.59
	Surface	0.48	-0.97	0.41

3.4.3 Specimens with 45-degree through-holes (TH-45)

In what follows, we compare measured experimental data with the corresponding results from parallel finite element simulations for cylindrical compression specimens with 45 degree through-holes (TH-45). Figure 3.12 compares experimental (DIC) and numerical (FEA) contour plots of the local axial strain on the surface of the specimen at different values of global compression $\Delta H/H$, where H is the length of the undeformed specimen and ΔH is the displacement of the actuated platen (which, in general, differs from the displacement d measured by the virtual extensometer). The bottom contour correlates to the DIC frame immediately prior to fracture initiation. The DIC strain field evolves from nearly homogeneous and axisymmetric at $\sim 2\%$ compression to strongly heterogeneous and non-

axisymmetric at $\sim 4\%$ compression, with significant regions of localization. The simulations are unable to capture this heterogeneity and circumferential variation in the axial strain field, and thus exhibit worsening agreement with increasing global compression. However, the simulation does capture the localization around the through-holes.

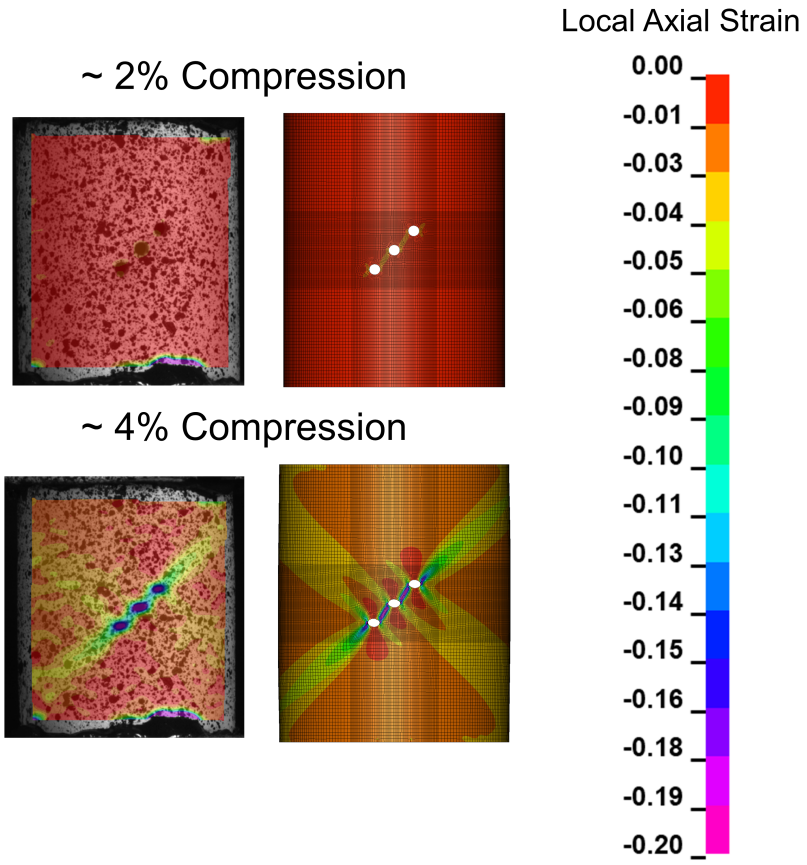

Figure 3.12: Local axial strain contours at $\sim 2\%$ (top) and $\sim 4\%$ (bottom) global compression from DIC (left) and FEA (right) for TH-V.

Figure 3.13 shows the force-displacement curves, as well as the maximum and minimum principal strain histories, for the cylindrical compression specimens with 45 degree through-holes (TH-45). The DIC principal strains are averaged over an area of interest on the specimen surface (Table 3.5). The FEA principal strains are averaged over a rectangular

area of elements bounded by the footprint of the corresponding DIC AOI. Agreement in force-displacement response is excellent for TH-45, with the simulation over-predicting force slightly in a single test. Agreement in principal strain histories is good, with the simulation over-predicting the maximum principal strain.

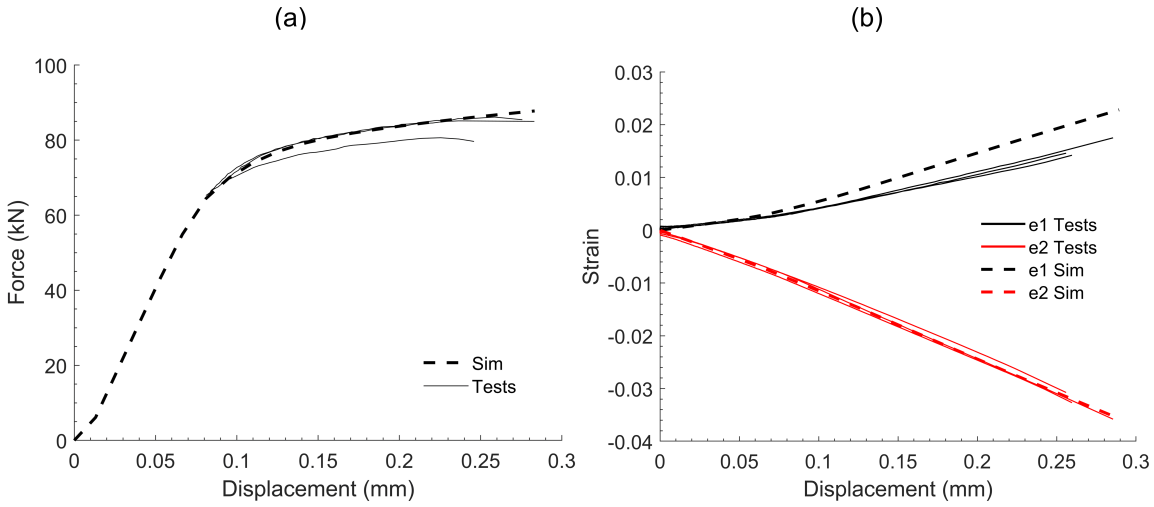

Figure 3.13: Comparison of experimental (measured) and numerical (simulated) (a) force-displacement response and (b) principal strain histories for TH-45 specimen.

With sufficient agreement between the measured experimental data and the corresponding simulation results, the stress state (triaxiality T and Lode parameter L) and equivalent plastic strain ($\bar{e}^p$) histories can be extracted from the numerical simulations at the location of fracture initiation. This is inferred from DIC images and post-mortem specimen inspection. However, there is inherent uncertainty in identifying the precise location of fracture initiation, and in particular, whether a fracture event initiated on the surface or interior of the specimen. To address this uncertainty, we report stress state histories at the geometric

center and free surface of the cylindrical compression specimen with 45 degree through-holes (TH-45). The fracture location for TH-45 appears to be at the mid-hole on the sides (Fig. 3.14). These locations on the mid-hole constitute an upper and lower bound, respectively, on the stress state, which varies nearly linearly (not shown) between the geometric center and free surface. For TH-45 specimens, the loading increases nearly linearly at the free surface (i.e., triaxiality and Lode parameter increase linearly with plastic strain accumulation). This also holds true at the geometric center of the specimen.

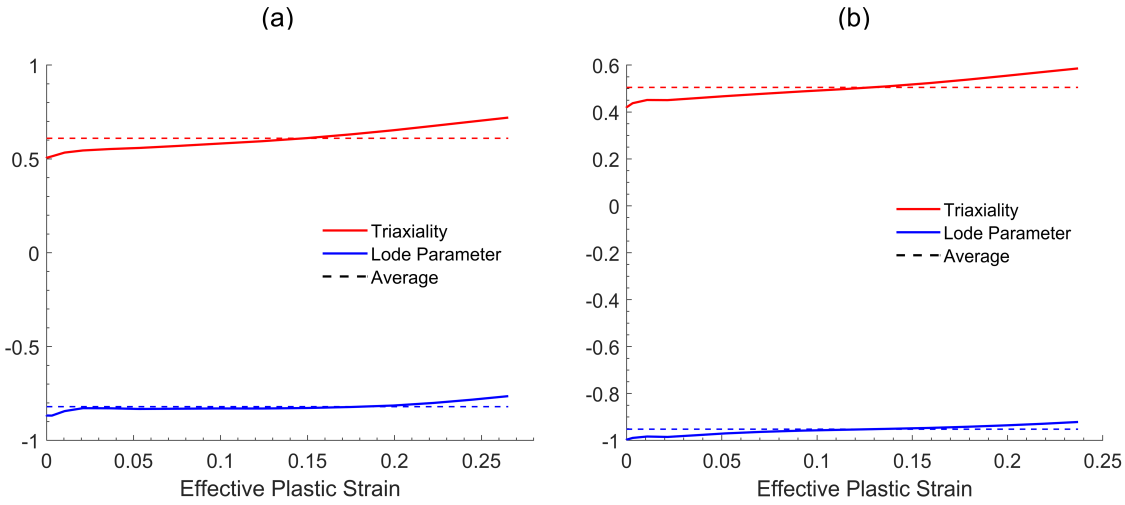

Figure 3.14: Evolution of stress state parameters with accumulated plastic strain at the (a) geometric center and (b) free surface of the TH-45 specimen.

Weighted averages of the triaxiality and Lode parameter are calculated for each test between the onset of plastic deformation and fracture initiation using Eq. 3.4. Table 3.11 reports the weighted average of the triaxiality T_{avg} and Lode parameter L_{avg} for cylindrical compression specimen with 45 degree through-holes. Also reported in Table 3.11 is the

equivalent plastic strain (EPS) at fracture $\bar{e}_f^p$. The EPS at fracture is slightly higher at the center of the specimens than at the free surface, which suggests a higher likelihood of fracture initiation in that location. At the geometric center, TH-45 gives a Lode parameter of -0.82, while the free edge gives a Lode parameter of -0.96; the triaxiality is significantly higher in the geometric center of the specimen (0.61 vs. 0.51), although both stress states are highly compressive. The equivalent plastic strain at fracture is slightly lower on the free edge of the specimen (24% vs. 27%).

Table 3.11: Weighted-average triaxiality, Lode parameter, and equivalent plastic strain at fracture for TH-45 specimen

Specimen		Triaxiality	Lode Parameter	EPS @ Fracture
TH-45	Center	0.61	-0.82	0.27
	Surface	0.51	-0.96	0.24

3.4.4 Specimens with horizontal through-holes (TH-H)

In what follows, we compare measured experimental data with the corresponding results from parallel finite element simulations for cylindrical compression specimens with horizontal through-holes (TH-H). Figure 3.15 compares experimental (DIC) and numerical (FEA) contour plots of the local axial strain on the surface of the specimen at different values of global compression $\Delta H/H$, where H is the length of the undeformed specimen and ΔH is the displacement of the actuated platen (which, in general, differs from the displacement d measured by the virtual extensometer). The bottom contour correlates to the DIC frame immediately prior to fracture initiation. The DIC strain field evolves from nearly homogeneous and axisymmetric at $\sim$ 5% compression to strongly heterogeneous and non-axisymmetric at $\sim$ 15% compression, with significant regions of localization. The

simulations are unable to capture this heterogeneity and circumferential variation in the axial strain field, and thus exhibit worsening agreement with increasing global compression. However, the simulation does capture the localization around the through-holes.

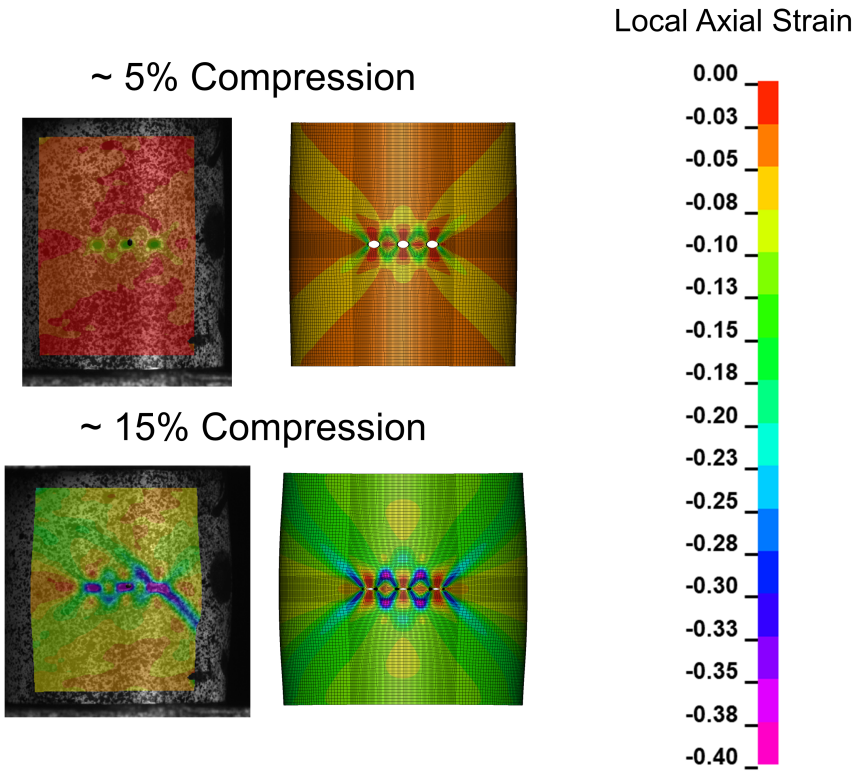

Figure 3.15: Local axial strain contours at $\sim$ 5% (top) and $\sim$ 15% (bottom) global compression from DIC (left) and FEA (right) for TH-V.

Figure 3.16 shows the force-displacement curves, as well as the maximum and minimum principal strain histories, for the cylindrical compression specimens with horizontal through-holes (TH-H). The DIC principal strains are averaged over an area of interest on the specimen surface (Table 3.5). The FEA principal strains are averaged over a rectangular area of elements bounded by the footprint of the corresponding DIC AOI. Agreement in

force-displacement response is excellent for TH-H. Agreement in principal strain histories is excellent, with the simulation falling within all tests curves.

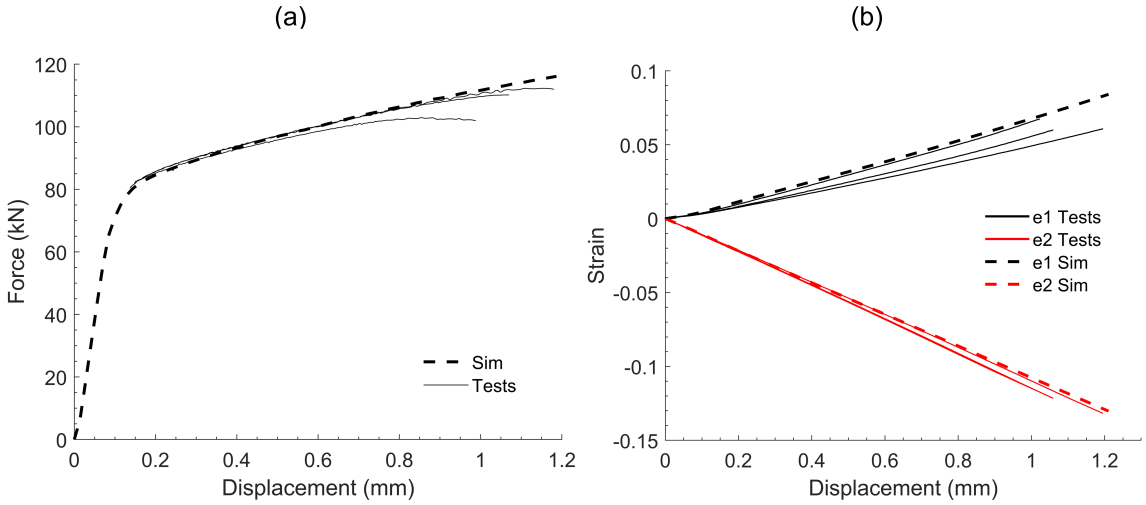

Figure 3.16: Comparison of experimental (measured) and numerical (simulated) (a) force-displacement response and (b) principal strain histories for TH-45 specimen.

With sufficient agreement between the measured experimental data and the corresponding simulation results, the stress state (triaxiality T and Lode parameter L) and equivalent plastic strain ($\bar{e}^p$) histories can be extracted from the numerical simulations at the location of fracture initiation. This is inferred from DIC images and post-mortem specimen inspection. However, there is inherent uncertainty in identifying the precise location of fracture initiation, and in particular, whether a fracture event initiated on the surface or interior of the specimen. To address this uncertainty, we report stress state histories at the geometric center and free surface of the cylindrical compression specimen with horizontal through-holes (TH-H). The fracture location for TH-H appears to be at the mid-hole on the sides

(Fig. 3.17). These locations on the mid-hole constitute an upper and lower bound, respectively, on the stress state, which varies nearly linearly (not shown) between the geometric center and free surface. For TH-45 specimens, the loading increases nearly logarithmically at the geometric center (i.e., triaxiality and Lode parameter increase logarithmically with plastic strain accumulation). The loading is nearly proportional at the free surface (i.e., triaxiality and Lode parameter vary only minimally with plastic strain accumulation) at the surface of the specimen

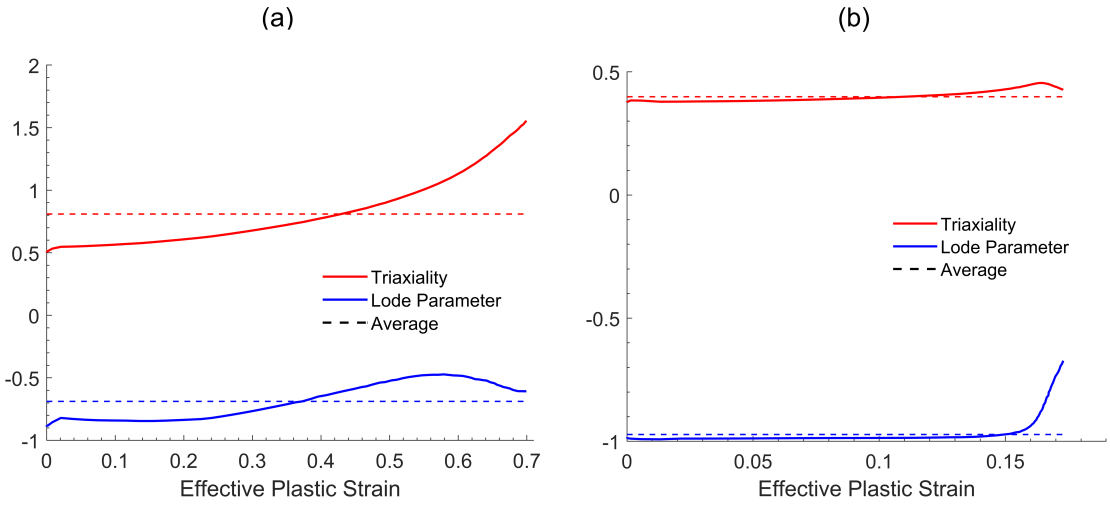

Figure 3.17: Evolution of stress state parameters with accumulated plastic strain at the (a) geometric center and (b) free surface of the TH-H specimen.

Weighted averages of the triaxiality and Lode parameter are calculated for each test between the onset of plastic deformation and fracture initiation using Eq. 3.4. Table 3.12 reports the weighted average of the triaxiality T_{avg} and Lode parameter L_{avg} for cylindrical compression specimen with 45 degree through-holes. Also reported in Table 3.12 is the

equivalent plastic strain (EPS) at fracture $\bar{e}_f^p$. The EPS at fracture is significantly higher at the center of the specimens than at the free surface, which suggests a higher likelihood of fracture initiation in that location. At the geometric center, TH-H gives a Lode parameter of -0.69, while the free edge gives a Lode parameter of -0.97; the triaxiality is significantly higher in the geometric center of the specimen (0.81 vs. 0.40), although both stress states are highly compressive. The equivalent plastic strain at fracture is significantly lower on the free edge of the specimen (17% vs. 70%).

Table 3.12: Weighted-average triaxiality, Lode parameter, and equivalent plastic strain at fracture for TH-H specimen

Specimen		Triaxiality	Lode Parameter	EPS @ Fracture
TH-H	Center	0.81	-0.69	0.70
	Surface	0.40	-0.97	0.17

3.4.5 Specimens with an spherical recess (SR)

In what follows, we compare measured experimental data with the corresponding results from parallel finite element simulations for cylindrical compression specimens with a spherical recess (SR). Figure 3.18 compares experimental (DIC) and numerical (FEA) contour plots of the local axial strain on the surface of the specimen at different values of global compression $\Delta H/H$, where H is the length of the undeformed specimen and ΔH is the displacement of the actuated platen (which, in general, differs from the displacement d measured by the virtual extensometer). The bottom contour correlates to the DIC frame immediately prior to fracture initiation. The DIC strain field evolves from axisymmetric with localization in the center of the specimen at $\sim 10\%$ compression to slightly heterogeneous and axisymmetric at $\sim 20\%$ compression, with significant regions of localization. The

simulations are unable to capture this heterogeneity and circumferential variation in the axial strain field, and thus exhibit worsening agreement with increasing global compression. However, the simulation does capture the localization around the spherical recess.

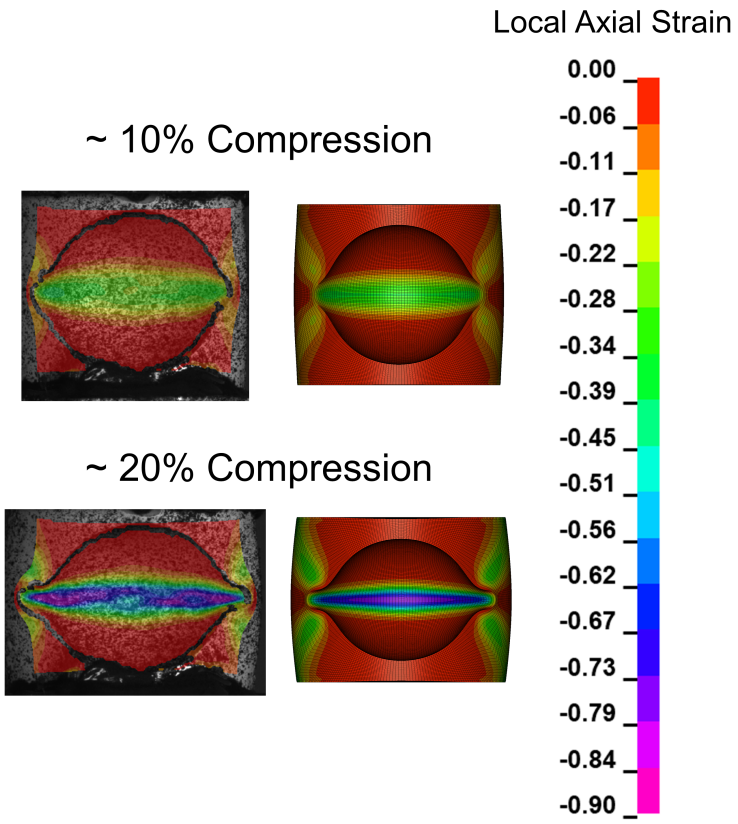

Figure 3.18: Local axial strain contours at $\sim$ 10% (top) and $\sim$ 20% (bottom) global compression from DIC (left) and FEA (right) for SR.

Figure 3.19 shows the force-displacement curves, as well as the maximum and minimum principal strain histories, for the cylindrical compression specimens with a spherical recess (SR). The DIC principal strains are *pointwise* values of e_1 and e_2 taken from a virtual strain gauge placed at the center (fracture initiation site) of the spherical recess (Table 3.5). The FEA principal strains are averaged over a rectangular area of elements located at the same

point as the DIC strain values with a length the same as the virtual strain gauge. Agreement in force-displacement response is excellent for SR. Agreement in principal strain histories is good, with the simulation slightly under-predicting the maximum principal strain.

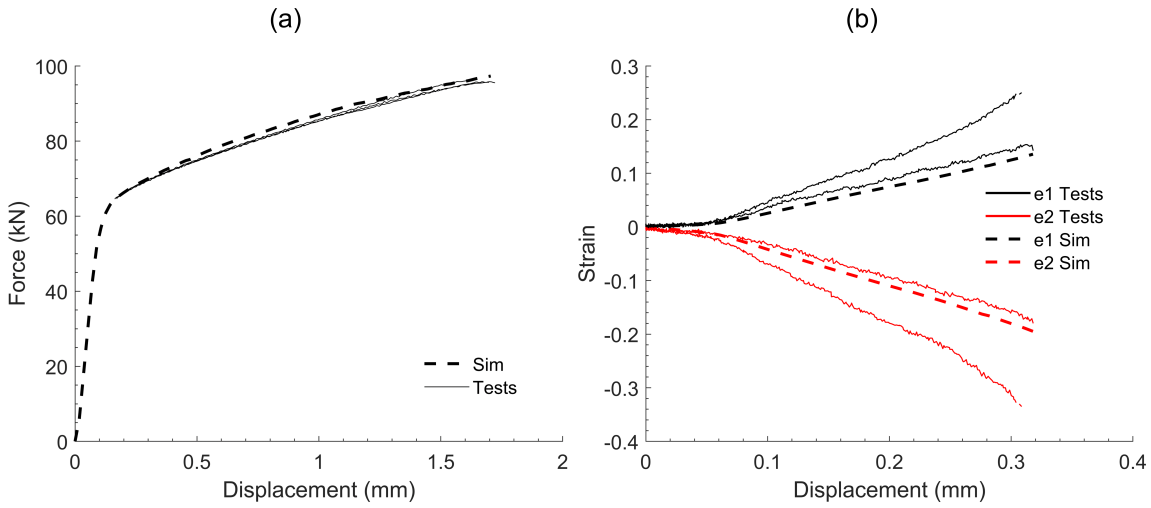

Figure 3.19: Comparison of experimental (measured) and numerical (simulated) (a) force-displacement response and (b) principal strain histories for SR specimen.

With sufficient agreement between the measured experimental data and the corresponding simulation results, the stress state (triaxiality T and Lode parameter L) and equivalent plastic strain ($\bar{e}^p$) histories can be extracted from the numerical simulations at the location of fracture initiation. This is inferred from DIC images and post-mortem specimen inspection. However, there is inherent uncertainty in identifying the precise location of fracture initiation, and in particular, whether a fracture event initiated on the interior surface of the spherical recess or edge of the spherical recess. To address this uncertainty, we report stress state histories at the interior surface of the spherical recess and the edge of the spherical

recess at the specimen's horizontal mid-plane (Fig. 3.20). These locations at the horizontal mid-plane constitute an upper and lower bound, respectively, on the stress state, which varies nearly linearly (not shown) between the geometric center and free surface. For SR specimens, the loading increases nearly linearly at the interior surface of the spherical recess (i.e., triaxiality and Lode parameter increase linearly with plastic strain accumulation). The loading is nearly proportional at the free surface (i.e., triaxiality and Lode parameter vary only minimally with plastic strain accumulation) at the edge of the spherical recess.

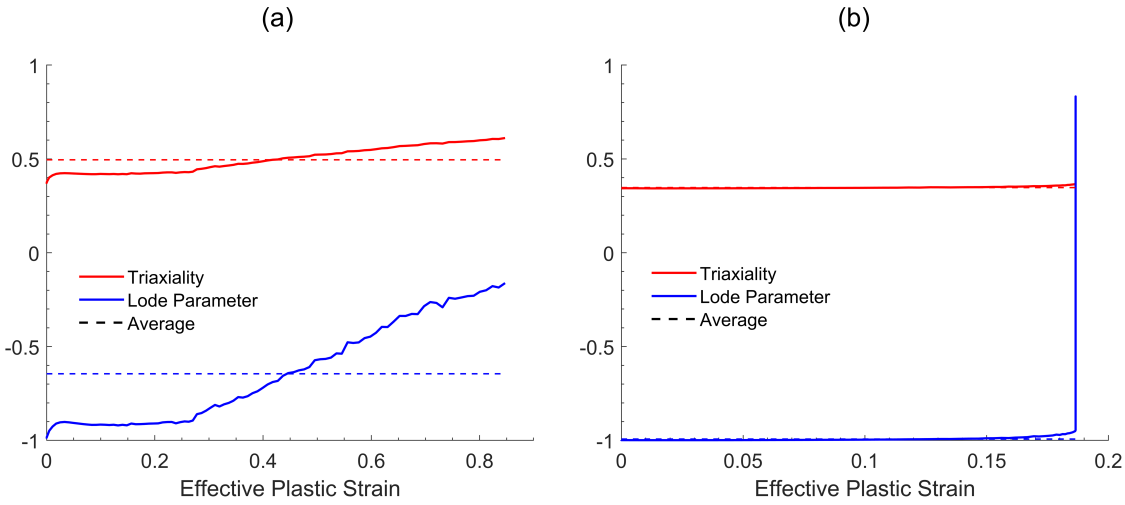

Figure 3.20: Evolution of stress state parameters with accumulated plastic strain at the (a) interior surface of the spherical recess and (b) edge of the spherical recess of the SR specimen.

Weighted averages of the triaxiality and Lode parameter are calculated for each test between the onset of plastic deformation and fracture initiation using Eq. 3.4. Table 3.13 reports the weighted average of the triaxiality T_{avg} and Lode parameter L_{avg} for cylindrical compression specimen with a spherical recess. Also reported in Table 3.13 is the equivalent

plastic strain (EPS) at fracture $\bar{e}_f^p$. The EPS at fracture is significantly higher at the interior surface of the spherical recess of the specimens than at the edge of the spherical recess, which suggests a higher likelihood of fracture initiation in that location. At the interior surface of the spherical recess, SR gives a Lode parameter of -0.65, while the edge of the spherical recess gives a Lode parameter of -1.0; the triaxiality is significantly higher in the interior recess of the specimen (0.50 vs. 0.35), although both stress states are highly compressive. The equivalent plastic strain at fracture is significantly lower on the edge spherical recess of the specimen (19% vs. 82%).

Table 3.13: Weighted-average triaxiality, Lode parameter, and equivalent plastic strain at fracture for SR specimen

Specimen		Triaxiality	Lode Parameter	EPS @ Fracture
SR	Interior Recess	0.50	-0.65	0.82
	Edge Recess	0.35	-1.00	0.19

3.4.6 Specimens with a 45-degree slot (S-45)

In what follows, we compare measured experimental data with the corresponding results from parallel finite element simulations for cylindrical compression specimens with a 45-degree slot (S-45). Figure 3.21 compares experimental (DIC) and numerical (FEA) contour plots of the local axial strain on the surface of the specimen at different values of global compression $\Delta H/H$, where H is the length of the undeformed specimen and ΔH is the displacement of the actuated platen (which, in general, differs from the displacement d measured by the virtual extensometer). The bottom contour correlates to the DIC frame immediately prior to fracture initiation. The DIC strain field evolves from homogeneous within the 45-degree slot at $\sim 1\%$ compression to slightly heterogeneous at $\sim 3\%$ compres-

sion, with significant regions of localization. The simulations are unable to capture this heterogeneity and circumferential variation in the axial strain field, and thus exhibit worsening agreement with increasing global compression. However, the simulation does capture the localization within the 45-degree slot. Note that the 45-degree slot is the only part of the specimen that strains.

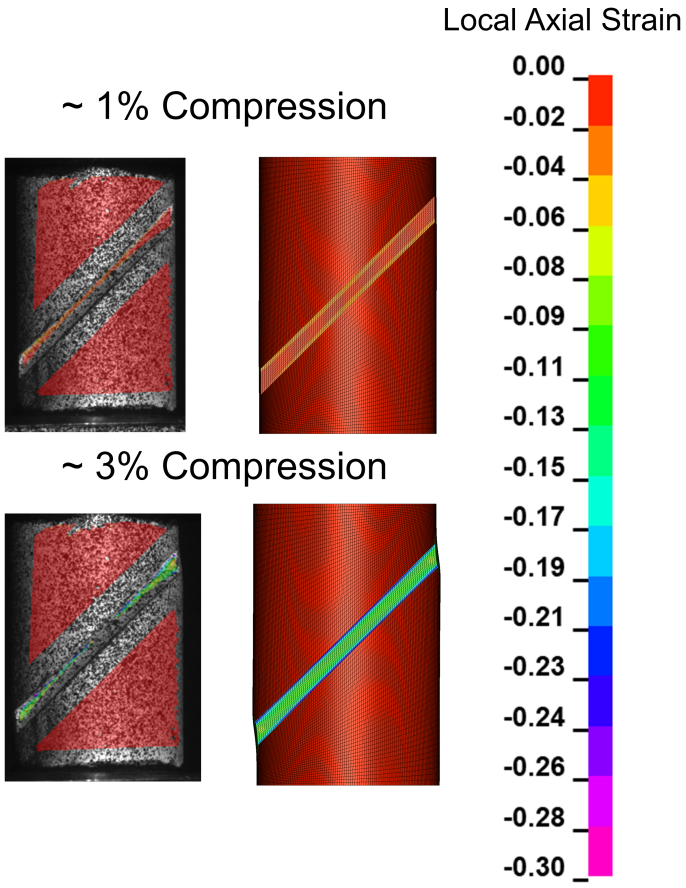

Figure 3.21: Local axial strain contours at $\sim$ 10% (top) and $\sim$ 20% (bottom) global compression from DIC (left) and FEA (right) for S-45.

Figure 3.22 shows the force-displacement curves, as well as the maximum and minimum principal strain histories, for the cylindrical compression specimens with a 45-degree slot

(S-45). The DIC principal strains are *pointwise* values of e_1 and e_2 taken from a virtual strain gauge placed at the center (fracture initiation site) of the 45-degree slot (Table 3.5). The FEA principal strains are averaged over a rectangular area of elements located at the same point as the DIC strain values with a length the same as the virtual strain gauge. Agreement in force-displacement response is excellent for S-45, with the simulation slightly over-predicting force. Agreement in principal strain histories is good, with the simulation slightly under-predicting the maximum principal strain.

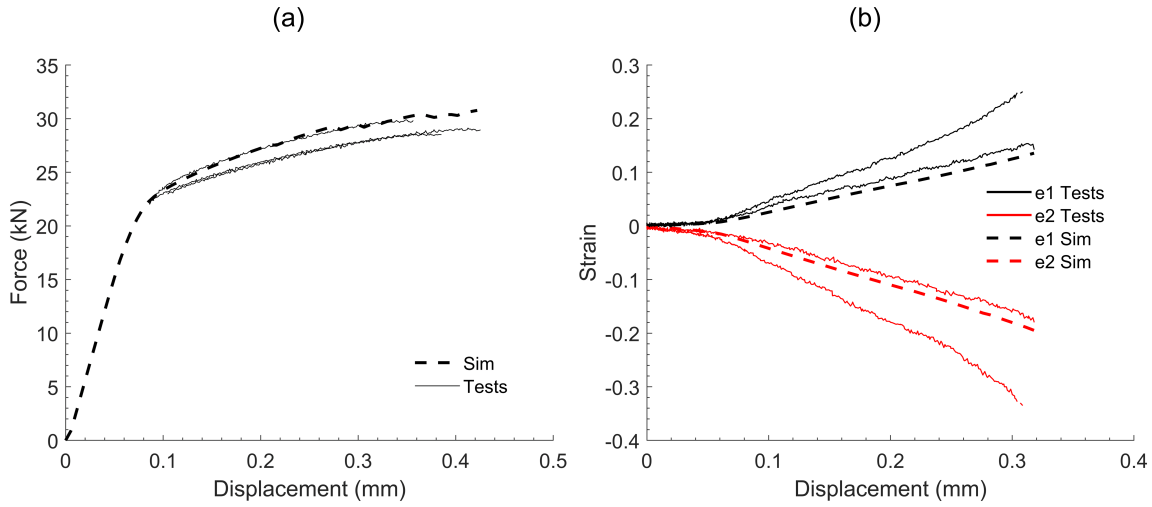

Figure 3.22: Comparison of experimental (measured) and numerical (simulated) (a) force-displacement response and (b) principal strain histories for S-45 specimen.

With sufficient agreement between the measured experimental data and the corresponding simulation results, the stress state (triaxiality T and Lode parameter L) and equivalent plastic strain ($\bar{e}^p$) histories can be extracted from the numerical simulations at the location of fracture initiation. This is inferred from DIC images and post-mortem specimen inspec-

tion. However, there is inherent uncertainty in identifying the precise location of fracture initiation, and in particular, whether a fracture event initiated on the interior of the 45-degree slot or the surface of the 45-degree slot. To address this uncertainty, we report stress state histories at the interior of the 45-degree slot and the surface of the 45-degree slot at the specimen's horizontal mid-plane (Fig. 3.20). These locations at the horizontal mid-plane constitute an upper and lower bound, respectively, on the stress state, which varies nearly linearly (not shown) between the geometric center and free surface. For S-45 specimen, the loading is nearly proportional at the interior of the 45-degree slot (i.e., triaxiality and Lode parameter vary only minimally with plastic strain accumulation). This also holds true at the surface of the 45-degree slot.

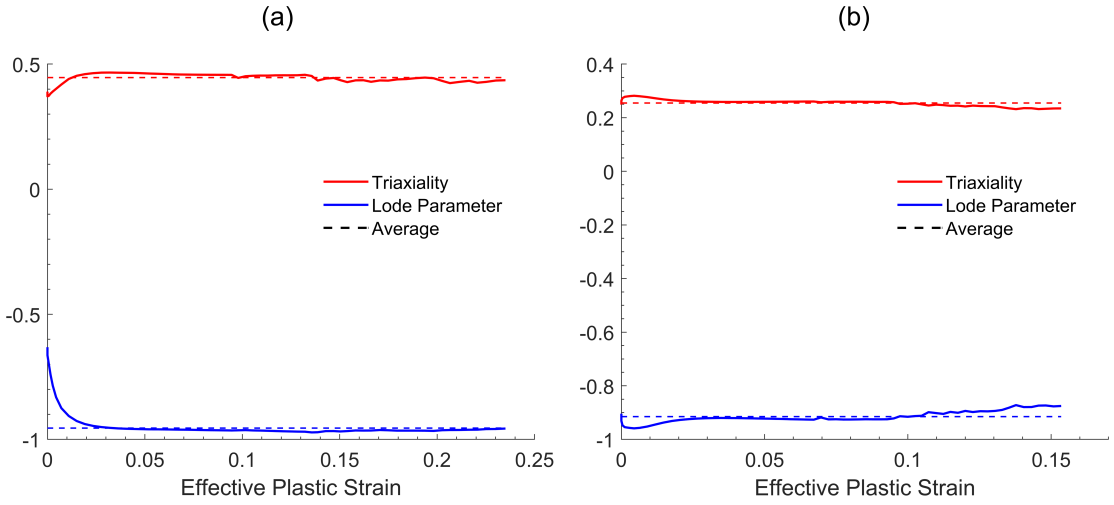

Figure 3.23: Evolution of stress state parameters with accumulated plastic strain at the (a) interior surface of the spherical recess and (b) edge of the spherical recess of the S-45 specimen.

Weighted averages of the triaxiality and Lode parameter are calculated for each test between the onset of plastic deformation and fracture initiation using Eq. 3.4. Table 3.14 reports the weighted average of the triaxiality T_{avg} and Lode parameter L_{avg} for cylindrical compression specimen with a 45-degree slot. Also reported in Table 3.13 is the equivalent plastic strain (EPS) at fracture $\bar{e}_f^p$. The EPS at fracture is significantly higher at the interior of the 45-degree slot of the specimens than at the surface of the 45-degree slot, which suggests a higher likelihood of fracture initiation in that location. At the interior surface of the 45-degree slot, S-45 gives a Lode parameter of -0.96, while the surface of the 45-degree slot gives a Lode parameter of -0.92; the triaxiality is significantly higher in the interior of the specimen (0.45 vs. 0.26), although both stress states are highly compressive. The equivalent plastic strain at fracture is significantly lower on the surface of the 45-degree slot of the specimen (15% vs. 24%).

Table 3.14: Mean of the Individual Tests Average Stress States

Specimen		Triaxiality	Lode Parameter	EPS @ Fracture
CS	Center	0.45	-0.96	0.24
	Surface	0.26	-0.92	0.15

3.4.7 Summary

Chapter III presents a comprehensive data set from an experimental program designed to achieve stress states in the compressive region of stress space. Compression tests of seven unique compression specimens compressed at a strain rate of 0.001 1/s are conducted. Each test goes to failure, and a fracture point is located using post-mortem and digital image correlation investigation. Each specimen is oriented with the longitudinal axis aligned with

the rolling direction. A custom MAT-224-GYS material model with a single tension and compression curve at a strain rate of 0.001 1/s is used in the finite element code LS-DYNA. The stress state is then taken from the element corresponding to the failure point in the experimental test. The stress states are then averaged using a weighted average up to the point of failure. The results show seven unique stress states in a previously unoccupied region of stress space. Figure 3.24 and Table 3.15 summarize all the tests presented in this chapter. Figure 3.24 also shows previous stress state points from the same 12.7-mm-thick Ti-6Al-4V plate [44].

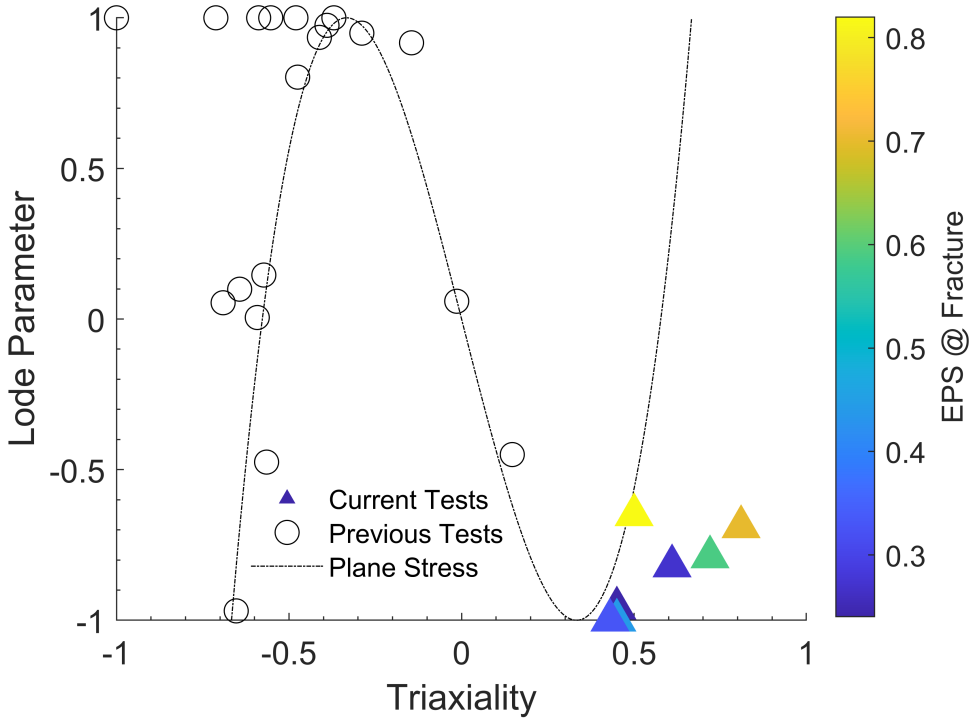

Figure 3.24: Stress space plot of all specimens (previous and current) tested on the 12.7-mm-thick Ti-6Al-4V plate.

Table 3.15: Stress States of All Tests

Specimen	Triaxiality	Lode Parameter	EPS @ Fracture
CC 1:1	0.45	-1.00	0.44
CC 1:2	0.43	-1.00	0.33
TH-V	0.72	-0.79	0.59
TH-45	0.61	-0.82	0.27
TH-H	0.81	-0.69	0.70
SR	0.50	-0.65	0.82
CS	0.45	-0.96	0.24

CHAPTER IV

CONCLUSIONS

4.1 Discussion, Recommendations, and Next Steps

An accurate finite element analysis material model is dependent on the development of a tabulated ductile fracture locus. While tabulating the ductile fracture locus is of the utmost importance, it is also crucial that the methodology used in this thesis is executed accurately. This methodology allows for multiple specimen configurations to be tested using the same test setup. Therefore, future work should be done using the same outlined methodology. However, there were several potential opportunities for improvement and refinement.

Certainty of fracture location is an opportunity for improvement. For the tests in this thesis, fracture location was determined by post-mortem and digital image correlation investigation. However, the digital image correlation image capture frequency (1 to 2 Hz) was not fast enough to capture the catastrophic failure of multiple specimens. For these specimens, post-mortem inspection was the only means to identify the fracture location. To solve this, we hypothesize that increasing the capture rate (adds computational time when processing DIC), or adding a high-speed camera capturing photos near the fracture event, could be done to more accurately capture the fracture location. Both of these options only help us when the fracture occurs on the surface of the specimen. To address whether fracture occurs on the surface or the geometric center of the specimens, fractography could be done.

Mesh effects must also be considered as an area for improvement. Although a general mesh refinement study was done, this did not include around fine features such as geometric irregularities. Around the irregularities (through-holes, spherical recess, 45-degree cut) the

mesh was finer than the rest of the specimen. However, this mesh may still not be fine enough, and a rigorous mesh convergence study should be performed. The mesh was created using a best practice guide, but there could still be room for improvement.

Digital image correlation was done on all tests, but some "drop-outs" were discovered. Around the edges of the spherical recess, inside the 45-degree slot, and around some of the through-holes, digital image correlation couldn't pick up some of the speckling. If failure occurred around the "drop-outs," the data calculated by digital image correlation, such as strains, may become less trustworthy. However, the principal strains between digital image correlation and finite element simulations match fairly well for all tests conducted.

In summary, extremely compressive stress-states produced from this test series populated a previously unpopulated area of the fracture locus. The triaxialities of 0.61, 0.72 and 0.81 are some of the most compression-dominated stress-states in the literature. These stress-states should increase the fidelity of the fracture locus for 12.7-mm-thick Ti-6Al-4V plate. However, there is still more work that can be done. Different geometric irregularities fine-tuned to achieve previously unachieved states of stress could be designed.

BIBLIOGRAPHY

[1] W. Emmerling, D. Altobelli, K. Carney, and M. Pereira, "Development of a new material model in ls-dyna—part 1: Faa, nasa, and industry collaboration background," *Federal Aviation Administration, Washington, DC, DOT/FAA/TC-13/25*, 2014.

[2] F. McClintock, "A criterion for ductile fracture by the growth of holes," *Journal of Applied Mechanics*, vol. 35, no. 2, pp. 363–371, 1968.

[3] J. Rice and D. Tracey, "On the ductile enlargement of voids in triaxial stress fields," *Journal of the Mechanics and Physics of Solids*, vol. 17, no. 3, pp. 201–217, 1969.

[4] A. L. Gurson, "Continuum theory of ductile rupture by void nucleation and growth: Part 1 - yield criteria and flow rules for porous ductile media," *Journal of Engineering Materials and Technology*, vol. 99, no. 1, pp. 2–15, 01 1977.

[5] V. Tvergaard and A. Needleman, "Analysis of the cup-cone fracture in a round tensile bar," *Acta metallurgica*, vol. 32, no. 1, pp. 157–169, 1984.

[6] T. Pardoen and J. Hutchinson, "An extended model for void growth and coalescence," *Journal of the Mechanics and Physics of Solids*, vol. 48, no. 12, pp. 2467–2512, 2000.

[7] A. Benzerga, J. Besson, and A. Pineau, "Anisotropic ductile fracture: Part i: Experiments," *Acta Materialia*, vol. 52, no. 15, pp. 4623–4638, 2004.

[8] K. Nahshon and J. Hutchinson, "Modification of the Gurson model for shear failure," *European Journal of Mechanics - A/Solids*, vol. 27, no. 1, pp. 1–17, 2008.

[9] G. R. Johnson and W. H. Cook, "Fracture characteristics of three metals subjected to various strains, strain rates, temperatures and pressures," *Engineering Fracture Mechanics*, vol. 21, no. 1, pp. 31–48, 1985.

[10] J. Hancock and A. Mackenzie, "On the mechanisms of ductile failure in high-strength steels subjected to multi-axial stress-states," *Journal of the Mechanics and Physics of Solids*, vol. 24, no. 2, pp. 147–160, 1976.

[11] A. Mackenzie, J. Hancock, and D. Brown, "On the influence of state of stress on ductile failure initiation in high strength steels," *Engineering Fracture Mechanics*, vol. 9, no. 1, pp. 167–188, 1977.

[12] O. Hopperstad, T. Børvik, M. Langseth, K. Labibes, and C. Albertini, "On the influence of stress triaxiality and strain rate on the behaviour of a structural steel. part i. experiments," *European Journal of Mechanics - A/Solids*, vol. 22, no. 1, pp. 1–13, 2003.

[13] T. Børvik, O. Hopperstad, and T. Berstad, "On the influence of stress triaxiality and strain rate on the behaviour of a structural steel. part ii. numerical study," *European Journal of Mechanics - A/Solids*, vol. 22, no. 1, pp. 15–32, 2003.

[14] Y. Bao and T. Wierzbicki, "On fracture locus in the equivalent strain and stress triaxiality space," *International Journal of Mechanical Sciences*, vol. 46, no. 1, pp. 81–98, 2004.

[15] Y. Bao, "Dependence of ductile crack formation in tensile tests on stress triaxiality, stress and strain ratios," *Engineering Fracture Mechanics*, vol. 72, no. 4, pp. 505–522, 2005.

[16] N. Bonora, D. Gentile, A. Pirondi, and G. Newaz, "Ductile damage evolution under triaxial state of stress: Theory and experiments," *International Journal of Plasticity*, vol. 21, no. 5, pp. 981–1007, 2005.

[17] D. Mohr and S. Henn, "Calibration of stress-triaxiality dependent crack formation criteria: A new hybrid experimental–numerical method," *Experimental Mechanics*, vol. 47, pp. 805–820, 2007.

[18] T. Wierzbicki, Y. Bao, Y.-W. Lee, and Y. Bai, "Calibration and evaluation of seven fracture models," *International Journal of Mechanical Sciences*, vol. 47, no. 4, pp. 719–743, 2005.

[19] I. Barsoum and J. Faleskog, "Rupture mechanisms in combined tension and shear—experiments," *International Journal of Solids and Structures*, vol. 44, no. 6, pp. 1768–1786, 2007.

[20] L. Xue, "Damage accumulation and fracture initiation in uncracked ductile solids subject to triaxial loading," *International Journal of Solids and Structures*, vol. 44, no. 16, pp. 5163–5181, 2007.

[21] Y. Bai and T. Wierzbicki, "A new model of metal plasticity and fracture with pressure and lode dependence," *International Journal of Plasticity*, vol. 24, no. 6, pp. 1071–1096, 2008.

[22] Y. Bai, "Application of extended Mohr–Coulomb criterion to ductile fracture," *International journal of fracture*, vol. 161, no. 1, pp. 1–20, 2010.

[23] T. B. Stoughton and J. W. Yoon, "A new approach for failure criterion for sheet metals," *International Journal of Plasticity*, vol. 27, no. 3, pp. 440–459, 2011.

[24] A. S. Khan and H. Liu, "A new approach for ductile fracture prediction on Al 2024-T351 alloy," *International Journal of Plasticity*, vol. 35, pp. 1–12, 2012.

[25] K. Danas and P. Ponte Castañeda, "Influence of the lode parameter and the stress triaxiality on the failure of elasto-plastic porous materials," *International Journal of Solids and Structures*, vol. 49, no. 11, pp. 1325–1342, 2012.

[26] L. Malcher and E. Mamiya, "An improved damage evolution law based on continuum damage mechanics and its dependence on both stress triaxiality and the third invariant," *International Journal of Plasticity*, vol. 56, pp. 232–261, 2014. [Online]. Available: https://www.sciencedirect.com/science/article/pii/S0749641914000035

[27] D. Mohr and S. J. Marcadet, "Micromechanically-motivated phenomenological Hosford–Coulomb model for predicting ductile fracture initiation at low stress triaxialities," *International Journal of Solids and Structures*, vol. 67-68, pp. 40–55, 2015.

[28] A. M. Beese, M. Luo, Y. Li, Y. Bai, and T. Wierzbicki, "Partially coupled anisotropic fracture model for aluminum sheets," *Engineering Fracture Mechanics*, vol. 77, no. 7, pp. 1128–1152, 2010.

[29] S. Haltom, S. Kyriakides, and K. Ravi-Chandar, "Ductile failure under combined shear and tension," *International Journal of Solids and Structures*, vol. 50, no. 10, pp. 1507–1522, 2013.

[30] J. Faleskog and I. Barsoum, "Tension–torsion fracture experiments—part i: Experiments and a procedure to evaluate the equivalent plastic strain," *International Journal of Solids and Structures*, vol. 50, no. 25, pp. 4241–4257, 2013.

[31] A. Ghahremaninezhad and K. Ravi-Chandar, "Ductile failure behavior of polycrystalline Al 6061-T6 under shear dominant loading," *International journal of fracture*, vol. 180, pp. 23–39, 2013.

[32] J. Papasidero, V. Doquet, and D. Mohr, "Ductile fracture of aluminum 2024-T351 under proportional and non-proportional multi-axial loading: Bao–Wierzbicki results revisited," *International Journal of Solids and Structures*, vol. 69-70, pp. 459–474, 2015.

[33] M. Scales, N. Tardif, and S. Kyriakides, "Ductile failure of aluminum alloy tubes under combined torsion and tension," *International Journal of Solids and Structures*, vol. 97-98, pp. 116–128, 2016.

[34] M. Scales, K. Chen, and S. Kyriakides, "Material response, localization, and failure of an aluminum alloy under combined shear and tension: Part i experiments," *International Journal of Plasticity*, vol. 120, pp. 340–360, 2019.

[35] Y. Bao and T. Wierzbicki, "On the cut-off value of negative triaxiality for fracture," *Engineering Fracture Mechanics*, vol. 72, no. 7, pp. 1049–1069, 2005.

[36] C.-K. Park, K. Carney, P. Du Bois, C.-D. Kan, D. Cordasco *et al.*, "Aluminum 2024-T351 input parameters for MAT-224 in LS-DYNA part 4: Ballistic impact simulations of a titanium 6Al-4V generic fan blade fragment on an aluminum 2024 panel using MAT-224 in LS-DYNA," United States. Department of Transportation. Federal Aviation Administration, Tech. Rep., 2021.

[37] Y. Lou, J. W. Yoon, and H. Huh, "Modeling of shear ductile fracture considering a changeable cut-off value for stress triaxiality," *International Journal of Plasticity*, vol. 54, pp. 56–80, 2014.

[38] N. Tutyshkin, W. H. Müller, R. Wille, and M. Zapara, "Strain-induced damage of metals under large plastic deformation: Theoretical framework and experiments," *International Journal of Plasticity*, vol. 59, pp. 133–151, 2014.

[39] P. Kubík, F. Šebek, J. Hůlka, and J. Petruška, "Calibration of ductile fracture criteria at negative stress triaxiality," *International Journal of Mechanical Sciences*, vol. 108-109, pp. 90–103, 2016.

[40] M. Brünig, S. Gerke, and M. Schmidt, "Damage and failure at negative stress triaxialities: Experiments, modeling and numerical simulations," *International Journal of Plasticity*, vol. 102, pp. 70–82, 2018.

[41] E. Jones and M. Iadicola, *A Good Practices Guide for Digital Image Correlation*. International Digital Image Correlation Society, 2018.

[42] LS-DYNA Aerospace Working Group, "Material parameter sets," 2025, accessed: 2025-05-02. [Online]. Available: https://awg.ansys.com/Material+Parameter+Sets

[43] J. T. Hammer, "Plastic deformation and ductile fracture of ti-6al-4v under various loading conditions," Master's thesis, The Ohio State University, 2012.

[44] S. Haight, L. Wang, P. Du Bois, K. Carney, and C.-D. Kan, "Development of a titanium alloy Ti-6Al-4V material model used in LS-DYNA," *FAA Report*, no. DOT/FAA/TC-15/23, 2016.

[45] D. Rittel, S. Lee, and G. Ravichandran, "A shear-compression specimen for large strain testing," *Experimental Mechanics*, vol. 42, no. 1, pp. 58–64, 2002.

[46] B. Knott, "Ductile fracture of aluminum 2024-T351, Ti-6Al-4V, and inconel 718 under complex states of stress," MS thesis, The Ohio State University, 2023.

APPENDIX A

Thin-Plate Experimental Program

Figures A.1 and A.2 show the force-displacement response and principal strain histories for all tests in the tests series.

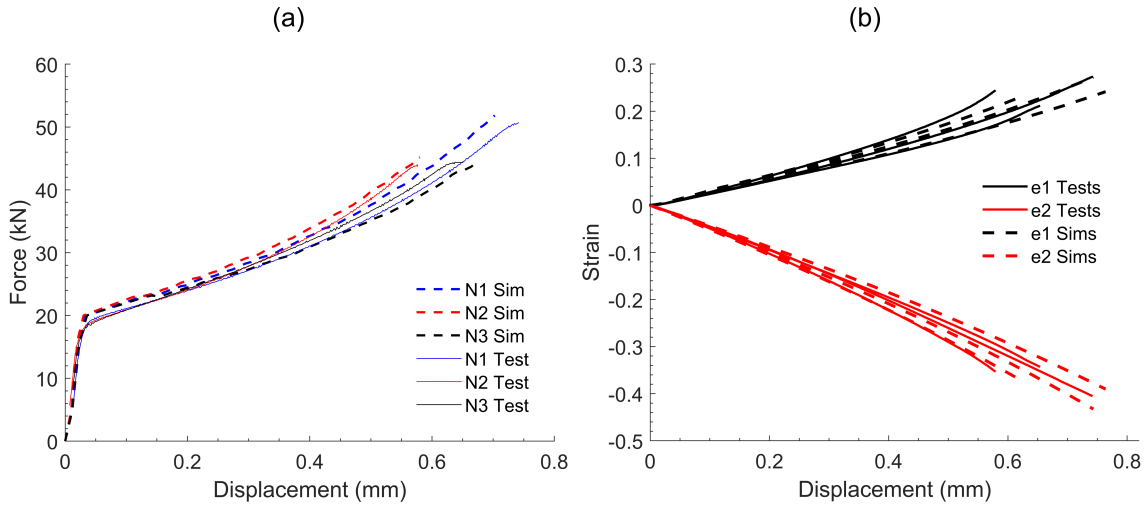

Figure A.1: Comparison of experimental (measured) and numerical (simulated) (a) force-displacement response and (b) principal strain histories for CC specimen with H/D = 1 for all tests.

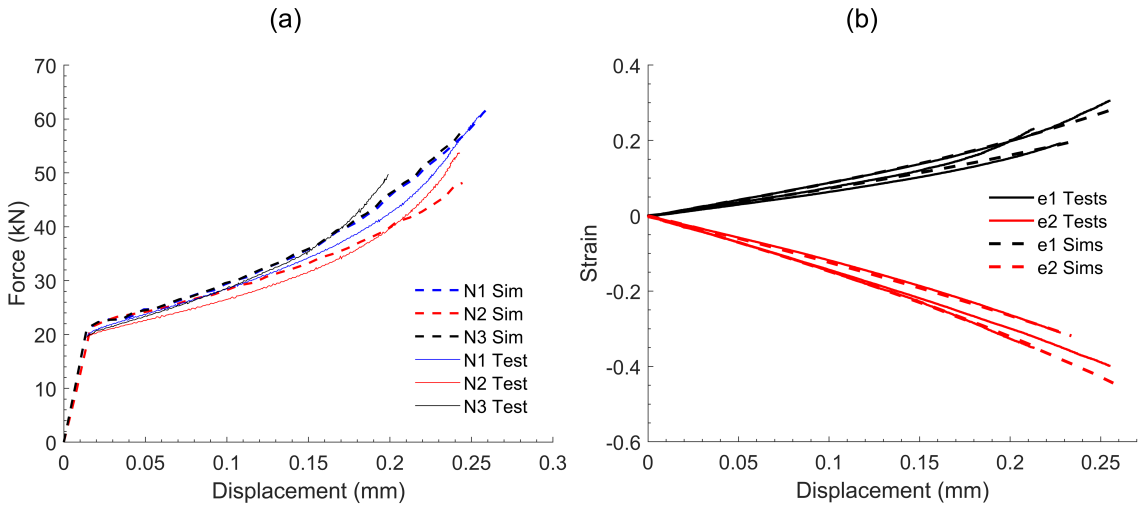

Figure A.2: Comparison of experimental (measured) and numerical (simulated) (a) force-displacement response and (b) principal strain histories for CC specimen with H/D = 0.5 for all tests.

APPENDIX B

Thick-Plate Experimental Program

Figure B.1 illustrates the specimens employed in the thick-plate ductile fracture experimental program.

These designs were adopted from Refs. [38, 39, 45].

Figures B.2 and B.3 show the force-displacement response and principal strain histories for all tests in the tests series.

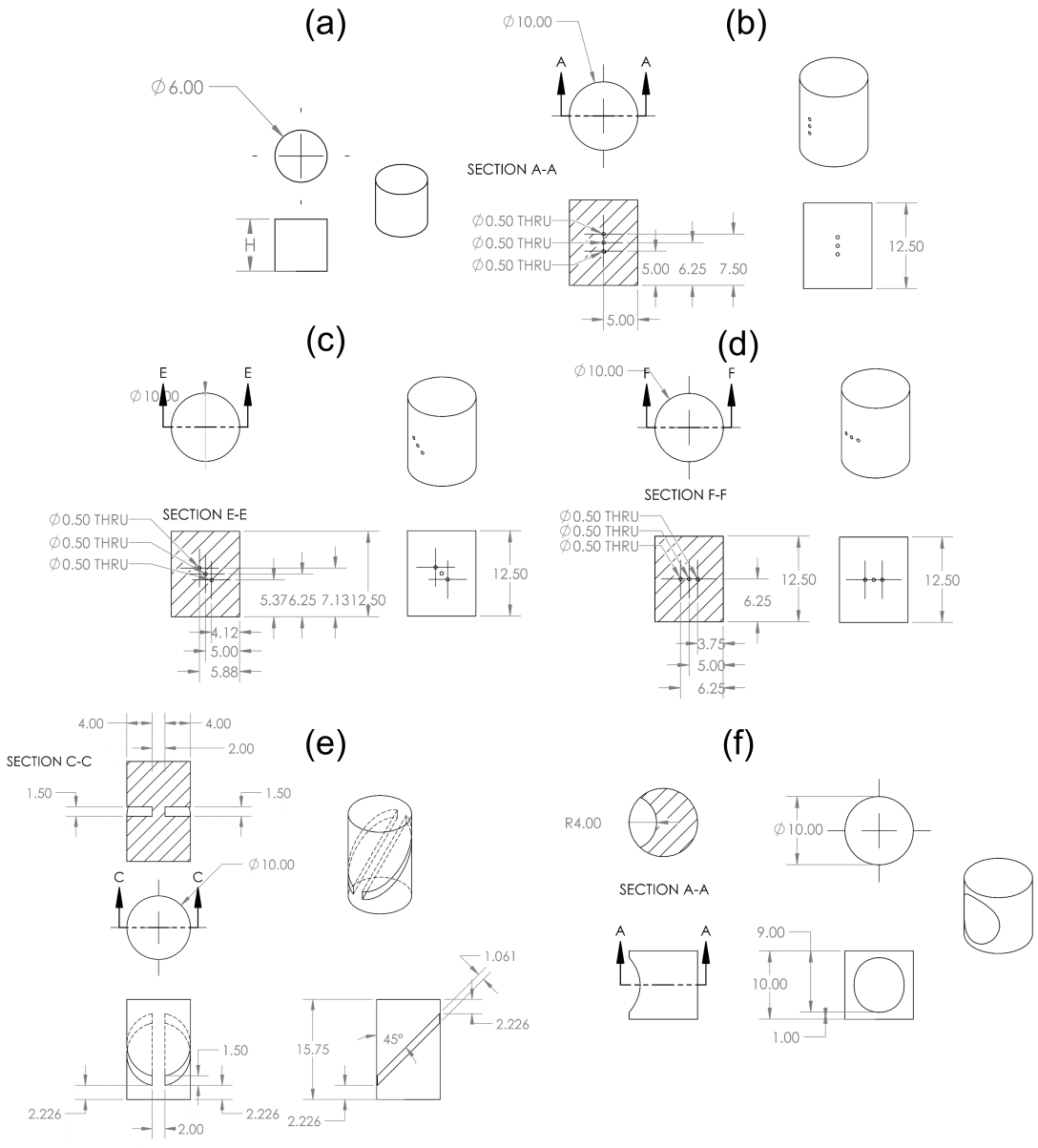

Figure B.1: Test specimens in the thick-plate experimental program. (a) Standard cylindrical compression (CC) specimens with length-to-diameter ratios of H/D = 1 and H/D = 0.5. Cylindrical compression specimens with (b) vertical through-holes (TH-V), (c) 45-degree through-holes (TH-45), (d) horizontal through-holes (TH-H), (e) a 45-degree slot (S-45), and a spherical recess (SR).

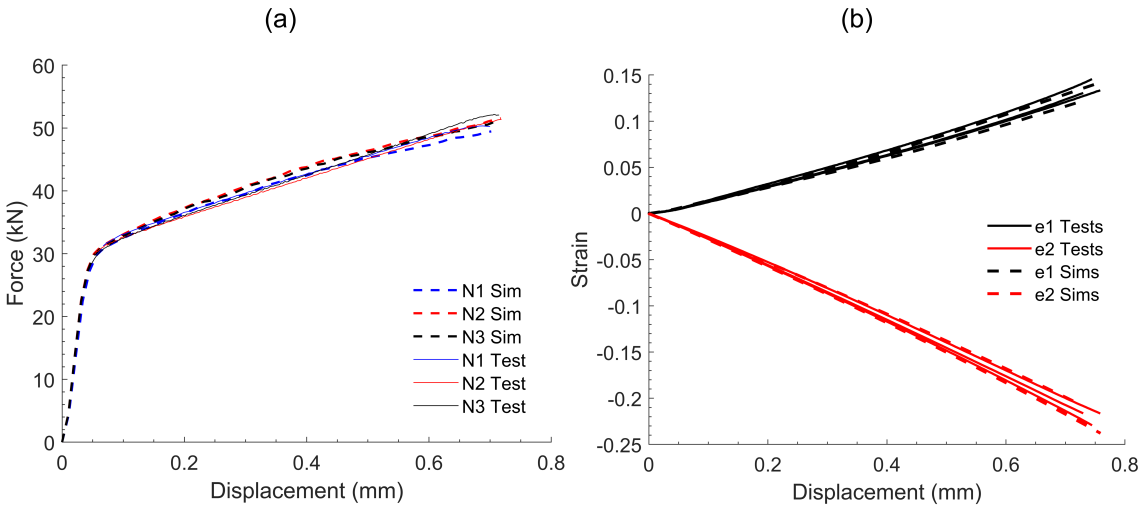

Figure B.2: Comparison of experimental (measured) and numerical (simulated) (a) force-displacement response and (b) principal strain histories for CC specimen with H/D = 1 for all tests.

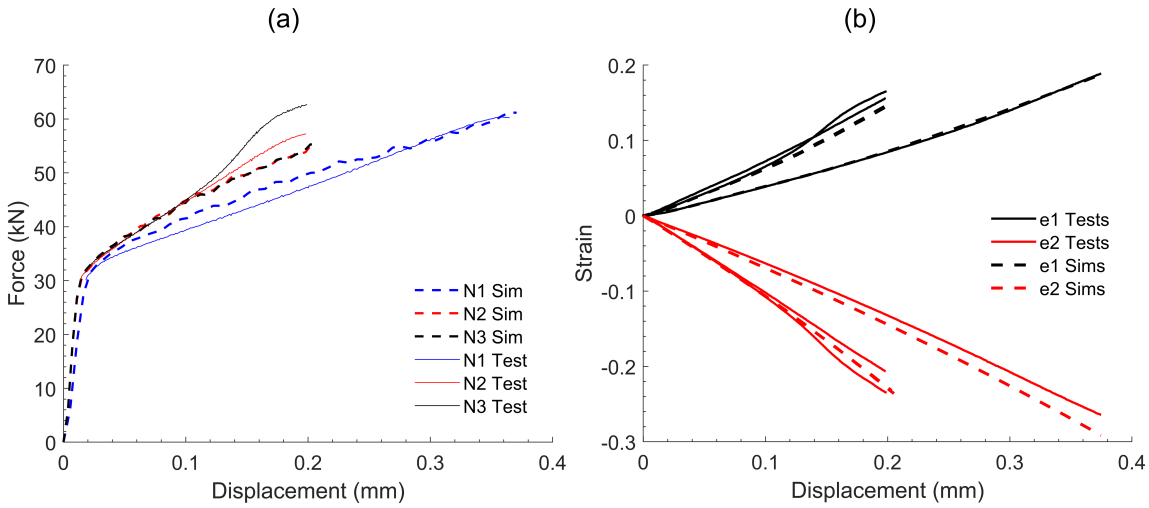

Figure B.3: Comparison of experimental (measured) and numerical (simulated) (a) force-displacement response and (b) principal strain histories for CC specimen with H/D = 0.5 for all tests.